Frictional slip weakening and shear-enhanced crystallinity in simulated coal fault gouges at subseismic slip rates

Caiyuan Fan[1], Jinfeng Liu[1,2,3], Luuk B. Hunfeld[4], Christopher J. Spiers[4]

[1]School of Earth Sciences and Engineering, Sun Yat-Sen University, Guangzhou, 510275, China
5 [2]Guangdong Provincial Key Lab of Geodynamics and Geohazards, Sun Yat-Sen University, Zhuhai, 519082, China
[3]Southern Marine Science and Engineering Guangdong Laboratory, Zhuhai, 519082, China
[4]Department of Earth Sciences, Utrecht University, Utrecht, 3584 CB, The Netherlands

Correspondence to: Jinfeng Liu (liujinf5@mail.sysu.edu.cn)

Abstract. Previous studies show that organic-rich fault patches may play an important role in promoting unstable fault slip.
10 However, the frictional properties of rock materials with near 100 % organic content, e.g. coal, and the controlling microscale mechanisms, remain unclear. Here, we report seven velocity stepping (VS) and one slide-hold-slide (SHS) friction experiments performed on simulated fault gouges prepared from bituminous coal, collected from the upper Silesian Basin of Poland. These experiments were performed at 25–45 MPa effective normal stress and 100 °C, employing sliding velocities of 0.1–100 $\mu m\ s^{-1}$, using a conventional triaxial apparatus plus direct shear assembly. All samples showed marked
15 slip weakening behaviour at shear displacements beyond ~1–2 mm, from a peak friction coefficient approaching ~0.5 to (near) steady state values of ~0.3, regardless of effective normal stress or whether vacuum dry flooded with distilled (DI) water at 15 MPa pore fluid pressure. Analysis of both unsheared and sheared samples by means of microstructural observation, micro-area X-ray diffraction (XRD) and Raman spectroscopy suggests that the marked slip weakening behaviour can be attributed to the development of R-, B- and Y- shear bands, with internal shear-enhanced coal crystallinity
20 development. The SHS experiment performed showed a transient peak healing (restrengthening) effect that increased with the logarithm of hold time at a linearized rate of ~0.006. We also determined the rate-dependence of steady state friction for all VS samples using a full rate and state friction approach. This showed a transition from velocity strengthening to velocity weakening at slip velocities >1 $\mu m\ s^{-1}$ in the coal sample under vacuum dry conditions, but at >10 $\mu m\ s^{-1}$ in coal samples exposed to DI water at 15 MPa pore pressure. This may be controlled by competition between dilatant granular flow and
25 compaction enhanced by presence of water. Together with our previous work on frictional properties of coal-shale mixtures, our results imply that the presence of a weak, coal-dominated patch on faults that cut or smear-out coal seams may promote unstable, seismogenic slip behaviour, though the importance of this in enhancing either induced or natural seismicity depends on local conditions.

Key words: slip-weakening, rate-dependent friction, frictional healing, strain localization, coal maturity, coal
30 **molecular structure**

1 Introduction

Carbonaceous materials (e.g. amorphous carbon, graphite, organic matters) are widely present in the lithosphere, including in several large fault zones over the world (Kaneki and Hirono, 2019), such as Longmenshan thrust belt in China (Kuo et al., 2014), Atotsugawa fault zone in Japan (Oohashi et al., 2012) and Alpine fault zone (Kirilova et al., 2017). As is well known

35   that graphite has very low friction strength, and that amorphous carbon or organic matters can be transformed into graphite at a seismic slip due to so-called graphitization process, the presence of carbonaceous materials may therefore act as a lubricant to play a key role in frictional properties and accordingly in promoting instability of the fault (Oohashi et al., 2011, 2013; Kuo et al., 2014). In the meanwhile, organic-rich rocks (such as coal, shale and clay), as main source rocks for (un)conventional natural gas, may also play a role in induced seismicity upon gas production (e.g. Kohli and Zoback, 2013;

40   Liu et al., submitted), water injection (e.g. Ellsworth, 2013) and coal mining (e.g. Westbrook et al., 1980). Compared to graphite, however, limited experimental data on frictional properties of organic-rich rocks, particular on coal, under in situ PT conditions is reported. Although coal has been widely investigated because of its importance in fuel energy and industry, its frictional properties are not yet well determined and understood. This contribution address frictional properties of coal and the likely mechanisms.

45

We first focus on coal structure and graphitization process seen in experiments. Many techniques, such as transmission electron microscope (TEM), nuclear magnetic resonance (NMR), X-ray diffraction (XRD), Raman spectroscopy, and Fourier Transform Infrared spectroscopy (FTIR), have been applied to determine coal structure, because of its complexity and heterogeneity (Li et al., 2015a, 2015b; Baysal et al., 2016; Song et al., 2019). From a chemical point view, coal, in

50   general, mainly consists of aromatic layers where aromatic nucleus are surrounded by peripheral aliphatic chains and oxygen functional groups (Mathews and Chaffee, 2012; Ahamed et al., 2019). Lu et al. (2001), based on XRD analysis of Australian coals ranging in rank from high volatile bituminous to semi-anthracite, proposed a simplified model for describing coal molecular structure. This model suggests coal consists of both amorphous (non-aromatic structures) and crystalline (a condensed, layered aromatic structure) forms of carbon. The aromatic layers in coal may become more ordered or more

55   uniform packing during deformation to form graphite under experimental conditions of a constant high confining pressure of 500 MPa, deviatoric stresses, variable temperatures of 300–600 °C and strains to 33 % (Ross and Bustin, 1990; Ross et al., 1991). Ross and the co-authors (1990; 1991), according to their experiments, reported that the shear strains associated with strain energy can drastically lower the activation energy and accordingly facilitate the graphitization process. Similarly, molecular dynamics simulations of sliding at the interface between amorphous carbon and diamond films, at a rate of 10 m s⁻

60   ^{1}, performed by Ma et al. (2014), show that covalent bond reorientation, phase transformation and structural ordering preferentially occur in localized bands in amorphous carbon film, and that this shear localization causes weakening. Apart from high pressure and temperature experiments, graphitization process has also seen in high-velocity friction experiments. Oohashi et al. (2011), for example, performed friction experiments on both amorphous carbon and graphite using a rotary

shear apparatus under conditions of normal stress of 0.5–2.8 MPa and slip rates of 50 μm s⁻¹ – 1.3 m s⁻¹ in atmospheres of air
65 and nitrogen. Their experiments showed a) a steady-state friction coefficient of 0.54 for amorphous carbon at slow slip rates
versus 0.1 for graphite at all slip rates, b) major slip-weakening of the amorphous phase, at slip rates >10 mm s⁻¹, to a steady-
state μ-value of 0.1, and c) XRD and TEM evidence of graphitization of the amorphous carbon during shear at high slip rates.
The authors suggested that large shear strains, short-lived flash heating, and/or stress concentrations at asperity contact
points may cause graphitization of amorphous carbon, even at low temperatures and pressures under anoxic environments.
70 Similar friction experiments, performed by Kuo et al. (2014) on natural samples collected from the 2018 Wenchuan
earthquake slip zone, also showed graphitization of carbonaceous minerals due to frictional heating at seismic slip rates.

We now return to frictional properties of coal. Recent research reported by Kaneki and Hirono (2019) investigated the
friction strength of lignite, bituminous coal, anthracite and graphite by performing high-velocity (1 m s⁻¹) rotary-shear
75 friction experiments at room temperature. They found that the peak friction strength, for all samples, decreased with
increasing maturity from 0.5 to 0.2, and the marked dynamic weakening was observed for lignite, bituminous coal and
anthracite, from peak values of ~0.3–0.5 to dynamic friction of ~0.1–0.2. TEM, IR and Raman spectra observations
performed on the samples before and after the friction experiments suggest that the marked dynamic weakening behaviour
observed in lignite, bituminous coal and anthracite was likely caused by shear-induced graphitization process which may be
80 dominated by flash heating (Kaneki and Hirono, 2019). On the other hand, in low-velocity friction experiments, our recent
research also found significant slip-weakening on simulated coal-rich fault gouge (Liu et al., submitted). We performed low-
velocity (i.e. 0.1–100 μm s⁻¹) direct shear experiments to investigate fictional properties of simulated fault gouges prepared
from coal-shale mixtures under (near) in situ PT conditions. We found that only the samples with coal volume fraction
≥50 %, including pure coal, showed marked slip-weakening behaviour, from peak value of ~0.47 to (near) steady-state value
85 of ~0.30, regardless of the employed experimental conditions. Interestingly, such slip-weakening is limited to small initial
displacements (2–3 mm), and does not occur during slip reactivation. We, based on the limited microstructure observation,
inferred this slip-weakening was caused by strain localization in coal-rich shear bands, accompanied by change in coal
molecular structure, as opposed to the graphitization effects seen in high-velocity friction experiments. As the main aim of
our recent research (Liu et al., submitted) was to investigate the effects of coal content on frictional properties of
90 Carboniferous shale in the context of induced seismicity in Carboniferous source rocks below Europe's largest gas field, we
only reported one velocity stepping friction experiments on pure coal. As a result, more experimental research is apparently
needed to better understand frictional properties (such as friction strength, rate-dependent friction and frictional healing) of
coal, sheared at subseismic slip rates under in situ PT conditions, accompanied by the development of coal molecular
structure upon shear deformation.
95

In this paper, we investigate the frictional behaviour of deep natural coal (as a source rock for (un)conventional natural gas)
under near in situ conditions. This was achieved by performing the friction experiments on simulated fault gouges prepared

from bituminous coal collected from the upper Silesian Basin of Poland. We performed velocity stepping and slid-hold-slide experiments under both vacuum dry and wet conditions, at a constant temperature of 100 °C, employing sliding velocities 0.1–100 μm s^{-1} and effective normal stresses ranging from 25 to 45 MPa. Data on the frictional strength and rate-dependence of friction are documented and a full Rate and State Friction (RSF) description is derived. In an attempt to understand the likely mechanisms determining frictional behaviour, post analysis was performed on both unsheared and sheared samples by means of microstructural observation, micro-area X-ray diffraction and Raman spectroscopy. Data on crystal structure parameters and Raman parameters are also obtained. Finally, we discuss the implications of our findings for understanding friction strength and seismic potential of coal-rich faults.

2 Experimental methods

2.1 Approach

Following Hunfeld et al. (2017) and Liu et al. (submitted), we performed direct shear experiments to measure the frictional sliding strength and rate-dependent friction of simulated coal fault gouges at near in situ PT conditions for deep coal seams. Post analysis by means of microstructural observation, micro-area XRD and Raman spectroscopy were performed on the deformed gouge samples, in an attempt to understand the observed frictional behaviour. In addition, we apply the rate and state friction (RSF) approach to determine the rate dependence of friction. From an RSF point view, if fault rocks exhibit an increase in frictional strength upon increased sliding rate, i.e. velocity strengthening behaviour, they are not prone to generating accelerating slip and are termed conditionally stable (Scholz, 2019). On the other hand, when the frictional strength of a fault rock decreases upon increased sliding rate, the fault rock exhibits velocity weakening behaviour. This may result in repetitive slip instabilities, or stick-slip events, which are viewed as the laboratory equivalent of earthquakes (Brace and Byerlee, 1966; Marone, 1998; Scholz, 1998).

2.2 Sample Materials

The coal samples used in this study were prepared from natural high volatile bituminous coal with total organic carbon (TOC) of 69.6 wt%, collected from Brzeszcze Mine (Seam 364) in the upper Silesian Basin of Poland (Hol et al., 2011; Liu et al., submitted). Petrological and chemical analyses reported by Hol et al. (2011) showed that the bituminous coal has a vitrinite reflectance of 0.77 ± 0.05 % and has a vitrinite content of 60.1 wt%, alongside liptinite 9.8 wt%, and inertinite 30.1 wt%. Furthermore, it contains 74.1 wt% carbon, 5.3 wt% hydrogen, 1.4 wt% nitrogen, 0.7 wt% Sulphur, 18.5 wt% oxygen, as well as 2.9 wt% moisture and 5.2 wt% ash (mineral) content. Raw coal sample was crushed to obtain powder with a grain size of <50 μm. For each experiment, a gouge layer with a thickness of ~1 mm (see details in Table 1) was prepared by compacting coal powders in a purpose-made die, at ~20 MPa for ~2 minutes. The gouge layer was then assembled into a "direct shear" assembly, comprising two opposing L-shape pistons, designed for direct shear testing in a triaxial deformation apparatus (following Samuelson and Spiers, 2012). Note that we marked starting, loose coal powders and one coal gouge sample

without shear deformation as S* and S0, respectively (see Table 1). They are used as the control samples for XRD and
130   Raman tests, in an attempt to determine the effects of shear/friction process on molecular structure of carbon in coal. Note
that the gouge sample S0 was prepared by compacting at ~20 MPa for ~15 h at 100 ℃.

2.3 Direct shear experiments and post-test sample treatment

We performed 8 direct shear experiments at a constant temperature of 100 ℃ using a conventional triaxial testing machine
(referred to as the Shuttle Machine, see Verberne et al., 2014a), equipped with the direct shear assembly described above. An
135   independent ISCO 65 volumetric (syringe) pump was used to control pore fluid pressure. A detailed description of the
machine was given by Verberne et al. (2014a) and Hunfeld et al. (2017). The experiments employed confining pressures (σ_n)
of 40, 50, 55 and 60 MPa, and a constant pore fluid pressure of P_f=15 MPa or under vacuum (i.e. P_f=0). Distilled (DI) water
was used as pore fluid for experiments S3–S8, while the experiments S1 and S2 were tested under vacuum dry (see Table 1
for details of experimental conditions). In each experiment, the sample assembly, initially drained to the lab air, was first
140   heated to ~100 ℃ at a confining pressure of ~20 MPa, and left to equilibrate for ~15 h (overnight). Then the pore fluid was
introduced into the sample and pressurized to 15 MPa at a confining pressure of ~20 MPa. The confining pressure was
subsequently increased to a certain value and left the system for ~3 h to equilibrate before shearing. Seven velocity-stepping
(VS) and one slide-hold-slide (SHS) experiments were conducted in this study (see Table 1). In the VS experiments, samples
were sheared at a constant velocity (V) of 1 μm s^{-1} for ~2.5 mm shear displacement, after which the loading rate was
145   instantaneously stepped in the range 0.1–100 μm s^{-1} over total displacement up to almost 6 mm. SHS experiment was also
performed at a constant velocity (V) of 1 μm s^{-1} interrupted by hold intervals in the range 300 to 30000 s, in attempt to
determine the healing effects of coal.

After each experiment, the direct shear setup was dismantled, and intact fragments of the sheared gouge layers were
150   recovered and oven-dried for several days. Note that, for SEM observation, to avoid the potential problem caused by use of
carbon-bearing epoxy, no special treatment was performed on the samples. Microstructure of the sheared samples S1–S8
were observed using optical microscope and SEM. For each sample, we chose the fragments that have clear, clean slip
surface, and the fragments that have relatively flat cross-section in an orientation parallel to the shear direction and
perpendicular to the shear plane (e.g. Fig. 1a). Micro-area XRD and Raman spectroscopy analysis were performed on
155   principal slip zone (PSZ) and weakly deformed zone (WDZ, terminology following Oohashi et al., 2011) of the samples S1–
S8 (e.g. Fig. 1c). Note that the surface of WDZ in Fig. 1c was exposed by scraping PSZ using abrasive paper. Recall that the
samples S* and S0 (i.e. without shear deformation), as control experiments, were also tested using XRD and Raman
spectroscopy. The location of the micro-area was selected randomly in PSZ, WDZ or unsheared surface, and was
schematically marked in Fig. 1b, c (blue circles).

160 **2.4 Post analysis**

2.4.1 Microstructural observation

A Leica EZ4w optical stereomicroscope and a table-top SEM fitted with an Energy Disperse Spectroscopy (EDS) were used to investigate the microstructure of the fragments retrieved from the deformed samples. Note that the fragments were not coated because coal samples have sufficient electroconductivity. The samples were imaged in the secondary electron mode,

165 using an acceleration voltage of 15–20 kV. In addition, EDS was used to determine whether the observed grains are coal or other minerals.

2.4.2 Micro-area XRD

We performed the micro-area XRD experiments on samples S0–S8 (except S2 and S6), in an attempt to determine the crystal structure of coal samples. Sample S* was tested by X-ray powder diffraction in a conventional mode. These were achieved

170 using the Smartlab 9 kW X-ray diffractometer with a Cu target at ambient temperature. Samples were scanned in 2θ range from 10 to 65° at a rate of 1° min^{-1}. The micro-area (~300 μm in diameter) in the PSZ and WDZ was measured for each sheared sample (see Fig. 1c). Note that the sample S*, S0 and S5 were measured twice for examining data reproducibility. For those samples, we took the average values as the parameters and the standard deviation as error bars.

2.4.3 Raman spectroscopy

175 We performed Raman measurements on samples S*–S8 to determine the development of coal maturity upon the shear/friction experiments. This was done using a Renishaw inVia™ laser Raman instrument (with a spectra resolution of 1 cm^{-1}) that was connected to a Leica DMLM microscope. The 514.5 nm argon-ion green laser was used for all experiments. The laser was focused through a ×50 objective, with a laser spot size of ~c.2 μm. We used a laser power of 0.2–1.0 mW (1 % – 5 % of ~17 mW full power) to avoid thermal damage on the targeted surface of coal samples. The scan range was limited

180 to 50–3000 cm^{-1}, in order to assess the first-order region and part of the second-order region. For each scan, we set the acquisition time of 10 s and the cumulative times of 3–5. For the unsheared and sheared samples (S0–S8), we measured three points randomly distributed in the unsheared or principal slip surface for each sample. Note that for the sample S4 only, we also measured 3 points in the weakly deformed zone. We accordingly took the mean values as the representative Raman parameters and the standard deviations as error bars for each sample. Note that we measured only one point in the powdered

185 sample S*.

2.5 Data acquisition, processing and analysis

2.5.1 Mechanical data

Internal axial force, confining pressure, pore fluid pressure, sample temperature and loading piston displacement were measured in each experiment and the signals logged using a 16-bit National Instruments AD converter and logging system

190 (for details, see Hunfeld et al., 2017). Following Liu et al. (submitted) and Hunfeld et al. (2017), the data were processed to yield sample shear stress versus shear displacement data corrected for machine stiffness (see details in Liu and Hunfeld, 2020). The frictional strength of the samples was characterised by defining the apparent coefficient of sliding friction (μ) as the ratio of sample shear stress (τ) over the effective normal stress (σ_n^{eff}), assuming zero cohesion.

$$\mu = \frac{\tau}{\sigma_n^{eff}} \tag{1}$$

195 where $\sigma_n^{eff} = \sigma_n - P_f$. Here σ_n represents the normal stress or confining pressure employed in the experiments, and P_f represents the pore fluid pressure.

The rate-dependence of friction was quantified using the RSF theory (Dieterich, 1979; Ruina, 1983), coupled with the empirical Dieterich-type "aging law" (e.g. Marone, 1998):

$$\mu = \mu_0 + a\ln\left(\frac{V}{V_0}\right) + b\ln\left(\frac{V_0\theta}{D_c}\right) \tag{2}$$

200 $$\frac{d\theta}{dt} = 1 - \frac{V\theta}{D_c} \tag{3}$$

which describes the evolution of friction coefficient μ from a reference steady state value (μ_0) towards a new steady state value, over a critical slip distance (D_c), in response to an instantaneous change in sliding velocity from an initial sliding velocity (V_0) to a new sliding velocity (V). θ is a state variable, commonly viewed as the average lifespan of a population of grain-to-grain contacts (Marone, 1998). At steady state, i.e. when $d\theta/dt = 0$, Eq. (2) reduces to:

205 $$(a - b) = \frac{\mu - \mu_0}{\ln\left(V/V_0\right)} \tag{4}$$

where the parameter (a-b) reflects the rate-sensitivity of friction coefficient. A positive (a-b) value indicates velocity strengthening behaviour, while a negative (a-b) value indicates velocity weakening behaviour, which is potentially unstable (Marone, 1998; Scholz, 1998). Here, we solve Eq. (2) simultaneously with an equation describing the elastic interaction with the testing machine via the stiffness, using Eq. (1) as a constraint. The values for a, b and D_c can then be obtained as the

210 solutions of a nonlinear inverse problem using an iterative least-squares minimization method (Ikari et al., 2009), thereby obtaining a full RSF description of the material from our experiments. In performing RSF inversion, departures from steady state frictional sliding were corrected for by means of linear detrending of hardening or softening behaviour (see Fig. 4a). A detailed description was also given by Blanpied et al. (1998).

2.5.2 Determining crystal structure parameters from XRD data

215   We first corrected for the background noise of the resulting diffractograms using a spline curve (see Fig. 2), obtaining an approximative profile of crystalline carbon (i.e. the background-subtracted intensity profile shown in Fig. 2). The obtained profile was further deconvoluted using Lorentzian and Gaussian function to determine the crystal structure parameters of coal. Specifically, Lorentzian peaks were first employed to determine minerals in 2θ range of ~16–30° (10–30° for powdered sample S*) and of ~35°–58°, in an attempt to remove the mineral peaks from the background-subtracted curve. We then

220   employed three Gaussian peaks to fit the background-subtracted, mineral-free profile at around 20°, 26° and 43°, obtaining γ-band, 002-band and 10-band, respectively (see Fig. 2). The fitting parameters, such as peak position (θ), full width at half maximum (β) and area (A), were obtained. Recall that here the crystalline carbon in coal means stacked aromatic layers or graphite-like structure. This is inferred from the presence of (002) band and broad (10) band in coal, which is similar to the (002) peak, (100) peak and (101) peak in graphite (Lu et al., 2001). On this basis, the crystal parameters of carbon crystallite

225   in coal, such as inter-layer spacing (d_{002}), crystallite stacking height (L_c), crystallite diameter (L_a), were determined using the empirical Braggs and Scherrer equations (Eqs. 5–7). Note that we took the mean values as the parameter for samples S*, S0 and S5.

$$d_{002} = \frac{\lambda}{2\sin\theta_{002}} \tag{5}$$

$$L_c = \frac{0.89\lambda}{\beta_{002}\cos\theta_{002}} \tag{6}$$

230   $$L_a = \frac{1.84\lambda}{\beta_{10}\cos\theta_{10}} \tag{7}$$

where λ is the wavelength of the applied X-ray (0.154056 nm for Cu Kα radiation); θ_{002}, β_{002}, θ_{10} and β_{10} represent the peak position of and full width at half maximum of bands (002) and (10) respectively. Theoretically, the areas of the bands (002) and (γ) (A_{002} and A_γ) are believed to be equal to the number of aromatic and aliphatic carbon atoms respectively (Yen et al., 1961), so that the aromaticity (f_a) of the samples can be estimated using Eq. (8). Coal rank can also be assessed using the

235   ratio of maximum intensity of (002) over that of (γ) band (I_{002}/I_γ, as seen in Eq. (9)).

$$f_a = \frac{A_{002}}{A_{002}+A_\gamma} \tag{8}$$

$$\text{Coal rank} = \frac{I_{002}}{I_\gamma} \tag{9}$$

2.5.3 Determining Raman parameters

Raman spectroscopy is a powerful tool for analyzing the information of molecular structure of organic matters (Ulyanova et
240   al., 2014). It is well known that G band, which is located around 1580 cm^{-1} in Raman spectra, is the only peak in first-order region (i.e. 900–2000 cm^{-1}) for pure single graphite crystal. D band is another peak located around 1350 cm^{-1} in Raman spectra, which is generally present along with G band for other carbon materials such as graphite with defective lattice, activated carbon and coal (Tuinstra and Koenig, 1970; Potgieter-Vermaak et al., 2011; Childres et al., 2013). The Raman

parameters for coal include the peak position, full width at half maximum (FWHM) and intensity of G and D band, the
245 Raman band separation (RBS = G-position - D-position), the intensity ratio of D-band over G-band (I_D/I_G) and the saddle
index (SI = the intensity of G-band divided by that of the saddle). These parameters can be obtained by several processing
methods (Beyssac et al., 2003; Sadezky et al., 2005; Wilkins et al., 2014; Henry et al., 2018; Khatibi et al., 2018). In this
paper, we use the method proposed by Henry et al. (2018) to determine the Raman parameters, as it has been well tested for
Carboniferous organic-rich mudstones and coals (Henry et al., 2019). In general, Henry's method include: a) The raw Raman
250 spectra was first smoothed using a Savitzky-Golay filter, i.e. a 21-point quadratic polynomial algorithm; b) A 3rd-order
polynomial function was then used to correct for baseline; c) The smooth, baseline-removed spectra was finally normalized
to a common G-band height of 2000 arb. units. Specifically, we used the automated Microsoft Excel® spreadsheet proposed
by Henry et al. (2018) to process our spectra data obtained at 900–2000 cm⁻¹.

3 Results

3.1 Mechanical data

Key data obtained from 8 direct shear experiments are listed in Table 1. All friction strength data are summarized, including
μ_{peak}, μ_{ss1} and μ_{ss2}. Here, μ_{peak} represents the peak friction coefficient obtained at 0.5–0.75 mm shear displacement, μ_{ss1} and
μ_{ss2} represent the near steady-state friction coefficient obtained at ~2.2 mm and ~5.7 mm shear displacement respectively.
The individual RSF parameters a, b and D_c, and the rate-sensitivity parameter (a-b), obtained in all velocity-stepping
260 experiments are summarized in Table 2.

3.1.1 Friction strength of simulated coal fault gouges

Typical apparent friction coefficients (μ) obtained in velocity stepping experiments (Exp. S1–S7) versus displacement are
plotted in Fig. 3. All experiments in Fig. 3a showed rapid, near-linear initial loading up to a peak friction coefficient,
subsequently followed by sharp, post-peak slip weakening from peak friction values (μ_{peak}) of ~0.48 to a near steady state
265 value ~0.3. The friction strength (μ_{peak} and μ_{ss1}) decreases with increasing effective normal stress, though this trend is not
significant (see Fig. 3b). The largest values for μ_{peak} (0.524) and μ_{ss1} (0.338) were obtained for the experiment S3, which was
performed at a confining pressure of 40 MPa and a pore water pressure of 15 MPa (i.e. at effective normal stress of 25 MPa).
Note that the values of μ_{peak} and μ_{ss1} obtained at vacuum dry condition (i.e. μ_{peak} of ~0.48 and μ_{ss1} of ~0.30 for experiments S1
and S2) are similar to (or slightly higher than) those (μ_{peak} = ~0.46 and μ_{ss1} = ~0.28) obtained for the samples S5 and S6 that
270 were exposed to DI water at the same effective normal stress of 40 MPa.

3.1.2 Rate dependence of friction

The (*a-b*) data obtained from the velocity stepping experiments S2–S7 represented in Fig. 3a, using a full RSF approach, are plotted in Fig. 4b as a function of applied stress states (σ_n, P_f). We here plot upward stepping data only, as it is these that are most relevant to rupture nucleation (Marone, 1998). Almost all (*a-b*) values are in the range of -0.006 to +0.002, and

275 systematically become smaller at higher velocity steps for all samples (see Fig. 4b). It is also seen from Fig. 4b that (*a-b*) values may not be sensitive to effective normal stress, but to velocity steps and pore fluids. Specifically, all samples behave velocity strengthening at velocity stepped from 0.1 to 1 μm s^{-1} (where *a-b*>0), but velocity weakening at the velocity stepped from 10 to 100 μm s^{-1} (where *a-b*<0). For the velocity stepped from 1 to 10 μm s^{-1}, the sample S2 tested under vacuum dry shows velocity weakening (i.e. *a-b*<0), while other samples tested with DI pore water at a pressure of 15 MPa show velocity

280 strengthening.

3.1.3 The frictional healing effects of coal

The slide-hold-slide loading path data (Exp. S8) shown in Fig. 5 indicates a clear but minor strength recovery or healing effect ($\Delta\mu$) upon re-shear, followed by slip-weakening to achieve a new quasi steady state. The magnitude of restrengthening ($\Delta\mu$) increases with the logarithm of hold time (*t*), and is well described by the equation $\Delta\mu = \beta\log(1+t/t_c)$ (e.g. Marone,

285 1998), where $\beta = 0.006 \pm 0.001$ and $t_c = 9 \pm 9$ s (Fig. 5b).

3.2 Microstructure of the deformed coal gouge

The representative microstructure for a sliding surface of sample S6 obtained using optical microscope in a reflected light mode is shown in Fig. 6a, indicating a highly reflective (mirrorlike) area located in the onset of the slip surface. This may be similar to the reported mirror slip surface (Siman-Tov et al., 2013; Fondriest et al., 2013; Verberne et al., 2014b). Besides, a

290 principal boundary slip zone (PSZ, of ~15−25 μm thick) accompanied with weakly deformed zone (WDZ) was observed in all deformed coal gouges (see Fig. 6b for a representative reflected light micrograph of the sample S1 in an orientation parallel to shear direction). Note that unlike boundary shear bands that were observed in all samples, R- and Y- shear bands were only observed in the sample S5 (see Fig. 6c). This may be because the surface of the fragments chosen from other samples were not flat enough to capture R- and Y- shear bands. In addition, SEM secondary electron images shown in Fig.

295 7a–e, may indicate the development of first microfractures inside the starting coal grains (~50 μm), then failure to form small grains (<10 μm) and finally shear bands. This likely reflects the process of cataclasis or granular flow during shear deformation in coal gouge (Niemeijer and Spiers, 2007; Verberne et al., 2014b; Hadizadeh et al., 2015). More importantly, a marked stack-layer structure was clearly observed at the margin of PSZ (see Fig. 7f), likely reflecting an interaction between PSZ and WDZ and the role of PSZ during friction process. This all indicates the development of first R shear, and then

300 boundary and Y shear bands, suggesting strain localization in the shear bands of coal gouge (terminology following Logan et al., 1992; Marone, 1998; Verberne et al., 2013).

3.3 Development of coal crystal structure

The raw X-ray diffractograms of the coal samples S*–S8 are presented in Fig. 8. Note that the diffractogram for coal powdered sample (S*) was scaled to a comparable size with other samples. Note also that the minor peaks observed in Fig. 8

305 represent minerals (such as kaolinite and dolomite) in coal samples. It is seen from Fig. 8 that a) high background intensity observed in all samples indicates a significant proportion of amorphous carbon (i.e. non aromatic system) in coal samples (Dun et al., 2013); b) The (002), (10) and γ-side bands of coal were also observed in all samples (see Fig. 8, following Hirsch, 1954 and Lu et al., 2001). Importantly, Fig. 8 demonstrates an apparent difference between unsheared (S* and S0) and sheared (S1–S8) samples, compared to that minor or little difference was observed between the sheared samples. This

310 strongly suggests the effects of shear/friction on development of molecular structure in coal. We also note that no graphite was formed after shear/friction processes.

Note that in this study we assume the crystalline carbon in coal, in general, consists of graphite-like layered aromatic structures plus marginal aliphatic structure (Lu et al., 2001). All structural parameters for carbon crystallite obtained using

315 the methods described in Sect.2.5.2 are listed in Table 3, and the representative structural parameters obtained from the samples S*–S8 were also plotted as a function of apparent steady-state shear stress associated with shear strain measured at shear displacement of ~5.7 mm in the direct shear experiments, as shown in Fig. 9. Specifically, the interlayer spacing (d_{002}) of the layered graphite-like structure in the sheared coal gouges yields 3.47–3.53 Å, including PSZ and WDZ, which is lower than (d_{002}) of 3.56–3.58 Å obtained for the unsheared samples S* and S0, as seen in Table 3 and Fig. 9a. This suggests the

320 layered graphite-like structures in coal, i.e. condensed aromatic system, became more condensed after shear/friction experiments. Careful inspection of Fig. 9a also indicates a thinner interlayer spacing (d_{002}) measured in PSZ compared to that measured in WDZ for most samples, suggesting the development of the layered graphite-like structures in boundary shear band during shear/friction processes. Similarly, the aromaticity (f_a), i.e. the ratio/fraction of aromatic carbon atoms, yields 0.44–0.49, 0.43–0.64 and 0.53–0.67 for the unsheared samples, WDZ and PSZ of the sheared samples, respectively (see

325 Table 3 and Fig. 9c). This also clearly indicates the development of the condensed aromatic system in coal upon shear/friction processes. The parameter (I_{26}/I_{20}), representative of coal rank, accordingly increased from 1.21–1.29 to 1.33– 2.29 after the shear/friction experiments. We also note that the stacked height of crystalline carbon (i.e. L_c) in coal, as seen in Table 3 and Fig. 9b, clearly increased from ~13 Å to ~20 Å after the shear/friction experiments. By contrast, the diameter of crystalline carbon (i.e. L_a) decreased from 20–21 to 15–19 Å after the shear/friction experiments (see Fig. 9b). We also note

330 that, for most samples, the values of L_c and L_a measured in WDZ lie in between that measured in the unsheared samples and PSZ of the sheared samples. In addition, it is seen from Fig. 9 that the structural parameters measured in the sheared samples, including PSZ and WDZ, seem to be insensitive to the applied effective normal stresses, the apparent steady-state shear stress and shear strain measured at shear displacement of ~5.7 mm.

3.4 Results of Raman spectra

335   The averaged normalized spectra of all samples after smoothing and background correction is plotted in Fig. 10. The D and
G bands were observed at ~1360 cm⁻¹ and ~1600 cm⁻¹ for all samples, respectively. Both D and G band observed in the
sheared samples are more narrow than those observed in the unsheared samples. In addition, the D band observed in the
sheared samples slightly shifted to the left, while the G band slightly shifted to the right, compared to those observed in the
unsheared samples. This likely reflects an increase in maturity of coal after the shear/friction experiments. The Raman
340   parameters described in Sect.2.5.3 were obtained from Fig. 10 and listed in Table 4. The Raman parameters for the samples
S0 and PSZ of S1–S8 were also plotted as a function of apparent steady-state shear stress associated with shear strain
measured at shear displacement of ~5.7 mm in the direct shear experiments, as shown in Fig. 11 a and b. It shows, in general,
an apparent difference in the Raman parameters between the sheared coal samples (S1–S8) and the unsheared sample S0,
suggesting the role of shear/friction. Particularly, G-FWHM values decrease from 91.3 cm⁻¹ measured in the unsheared
345   sample to 71.7–79.7 cm⁻¹ measured in the sheared samples. RBS and SI values increase from 227.7 cm⁻¹ and 3.27 measured
in the unsheared samples to 239.3–256.7 cm⁻¹ and 3.65–4.26 measured in the sheared samples. By contrast, we found similar
parameter values of I_D/I_G for all samples, yielding 0.543–0.561, which is not sensitive to the shear deformation. It is also
seen from Fig. 11 a and b that all Raman parameters measured in the sheared samples are not sensitive to the applied
effective normal stress, and apparent steady-state shear stress and shear strain. Recall that we measured Raman spectra in
350   WDZ only for the sample S4. We plotted the Raman parameters measured in samples S*, S0 and S4 in Fig. 11 c and d,
indicating slight difference between WDZ and PSZ, as well as the difference between S* and S0.

4 Discussion

We have documented 8 direct shear experiments performed on simulated gouge samples prepared from natural bituminous
coal. The experiments were conducted at a constant temperature of 100 ℃ to investigate frictional properties of coal exposed
355   to DI water and vacuum dry at effective normal stress of 25–45 MPa. The experimental conditions, frictional strength and
rate-dependent friction of all experiments are listed in Tables 1 and 2. All experiments show significant slip-weakening
behaviour, from a peak friction coefficient of ~0.5 to a near steady state value of ~0.3. Post microstructure observation
indicated the development of shear bands. In addition, XRD and Raman analysis suggest the shear deformation may change
the molecular structure and maturity of coal in the shear bands. Furthermore, the VS experiments showed that a) little effect
360   of effective normal stress on friction strength and (*a-b*) values were found; b) (*a-b*) values systemically become smaller at
higher velocity steps; c) the samples exposed to DI water at a pore pressure of 15 MPa exhibited velocity strengthening
behaviour at velocity steps of 0.1–10 μm s⁻¹, but velocity weakening behaviour at velocity steps of 10–100 μm s⁻¹, as
opposed to the sample under vacuum dry that showed velocity weakening behaviour at almost all velocity steps employed in
this study. The SHS experiment demonstrated minor frictional healing (β=0.006 ± 0.001) in a water-saturated coal gouge
365   sample. In the following, we first attempt to elucidate the development of molecular structure of coal upon shear deformation.

We then discuss whether the shear-induced molecular structure change dominated the marked slip-weakening behaviour observed in coal gouges. We also discuss the velocity or rate dependent friction of coal. Finally, we consider, in a broad way, the implications of our findings for the frictional strength and (induced) seismic potential of coal-rich or organic-rich faults.

4.1 Development of molecular structure and maturity of coal in the shear bands and its cause

370   Following Lu et al. (2001), we assume our bituminous coal consists of graphite-like crystalline (i.e. a condensed aromatic system) and amorphous (i.e. non-aromatic system) forms of carbon. Our XRD results on the unsheared samples (S* and S0) show the structure of the graphite-like crystalline carbon in bituminous coal, yielding the interlayer spacing (d_{002}) of ~3.56 Å, the crystallite diameter (L_c) of ~13.5 Å, the stacked height (L_a) of ~19 Å, and aromaticity (f_a) of ~0.47. These parameter values are consistent with those of the similar bituminous coal reported by K. Li et al. (2015a), Okolo et al. (2015) and

375   Zhang et al. (2015). Note that the parameter values of d_{002}, L_c and L_a that were calculated using Scherrer's equation may be larger than the real size (Lu et al. 2001), and that the presence of mineral peaks particularly in the 2θ range of 27–50° may also influence the fitting process (i.e. fitting Gaussian peak to (002), (γ) and (10) band), and may accordingly influence the accuracy of the structural parameter values. However, these influences should be consistent for all samples. We therefore believe the values of the structural parameters shown in Table 3 and Fig. 9 could be influenced by these factors as a systemic

380   error and accordingly would not change the trend or results that we observed in Fig. 9. Furthermore, the minor standard deviations shown in the measurements on samples S*, S0 and S5 indicate a good reproduction of our XRD measurements. As a result, we believe that our XRD results on both unsheared and sheared samples, particularly on PSZ, indeed demonstrate the structure of graphite-like crystalline carbon became more uniform after the shear/friction experiments, i.e. d_{002} became smaller, while L_c, f_a and I_{26}/I_{20} became larger (see Fig. 9 and Table 3). This development of molecular structure

385   likely reflects an increase in maturity of the coal samples after the shear/friction experiments, which is in good agreement with our observations from Raman spectra. As is known that many Raman parameters are correlated with maturity index (such as vitrinite reflectance (VR) and total fixed carbon), and the correlations are widely reported (Wilkins et al., 2014; Schito et al., 2017; Henry et al., 2018, 2019; Zhang and Li, 2019). Generally, G-FWHM, D-FWHM and I_D/I_G are negatively related to measured %VR, while RBS and saddle index are opposite. To better illustrate the change in coal maturity upon

390   shear/friction experiments from our Raman spectra, we plotted two representative correlations between Raman parameters and maturity reported by Henry et al. (2019b) in Fig. 11a, i.e. G-FWHM vs. VR and RBS vs. VR. It is clearly seen in Fig. 11a that the apparent differences in Raman parameters (G-FWHM and RBS) between the sheared and unsheared samples show that the coal maturity was improved after the shear/friction experiments. We also note that the petrological and chemical analyses showed our coal sample has a vitrinite reflectance of 0.77 ± 0.05 %, which is larger than the values of VR

395   of the unsheared sample S* (~0.6) and S0 (~0.4–0.5) obtained from the correlations shown in Fig. 11a. This suggests it would be difficult to quantitively determine the maturity increase upon the shear/friction process using these correlations between Raman parameters and VR. Nonetheless, these correlations shown in Fig. 11a, we believe, have demonstrated that

the Raman parameters can reflect coal maturity change, and once again, the change in Raman parameters accordingly indicates an increase in coal maturity upon shear/friction experiments.

400

We now attempt to elucidate the likely mechanisms responsible for the development of molecular structure and maturity of coal during the shear/friction process. It is well known that molecular structure and maturity of coal would be changed under conditions of high temperature and pressures at a geological timescale during metamorphism (Bonijoly et al., 1982; Oberlin, 1984; Buseck and Huang, 1985; Buseck and Beyssac, 2014). Research on pyrolysis of bituminous coal showed that, when

405 temperature is below ~200 ℃, volatilization of small molecules and slight breaking of aliphatic chains would occur to produce only trace amounts of gas (e.g. CO and/or CH_4), while above ~300–400 ℃, the amount of most functional groups would decrease rapidly with the cracking of C-H bonds and C-C bonds, generating much gas (Öztaş and Yürüm, 2000; Zhao et al., 2007; Niu et al., 2016; Kaneki et al., 2018). Besides, high resolution TEM, Raman spectroscopy and FTIR analysis performed on the tectonically deformed coals, which often accumulate many shear strains associated with strain energy,

410 suggest that tectonic deformation can improve the ordering of aromatic structure and reduce the content of hydrogen and oxygen (Ju et al., 2005; Cao et al., 2007; Xu et al., 2014; Pan et al., 2017; Song et al., 2018). Therefore, returning to our experiments, under the PT conditions employed (i.e. 25–45 MPa effective normal stress and 100 ℃), we believe, the molecular structure of bituminous coal is very unlikely to be changed over hours without the shear/friction process (Hou et al., 2014; Xu et al., 2014). Moreover, the slip rates (0.1–100 μm s^{-1}) employed in our experiments means the development of

415 molecular structure and maturity due to sample-scale frictional heating effects seen in high-velocity friction experiments can be eliminated (Rice, 2006; Di Toro et al., 2011; Aharonov and Scholz, 2018). In addition, we infer that flash heating mechanisms reported by Kaneki and Hirono (2019) may play little or minor role, as the structural and Raman parameters are both insensitive to applied effective normal stress. As a result, we infer that the improvement of molecular structure and maturity observed in our experiments is caused by shear deformation (i.e. strain localization in the shear bands) associated

420 with strain energy (Hou et al., 2017). Similarly, an improvement of molecular structure of anthracite coal was also observed in the creep compaction experiments at axial strain rates of 1.3×10^{-6}–1.3×10^{-4} s^{-1}, performed at a confining pressure of 500 MPa and at temperatures of 300–600 ℃ (Ross et al. (1990; 1991). Ross and co-authors (1990; 1991), based on TEM observations on the deformed samples, found that stacks of aromatic layers in coal became more ordered and was progressively aligned in the plane of flattening during deformation, i.e. the organization of crystalline carbon was

425 significantly improved during the deformation, but not enough to form graphite. Aside from creep compaction experiments, Bustin et al. (1995a, 1995b) also performed simple shear experiments at a confining pressure of 0.8 or 1 GPa on bituminous and anthracite coal at temperatures of 400–900 ℃ employing shear strain rates of 1×10^{-5}–1×10^{-6} s^{-1}, as opposed to our shear strain rates of ~1×10^{-4}–1×10^{-1} s^{-1} and PT conditions. They found, only for the sheared samples, graphite was formed from bituminous coal initially at 800 ℃ and commonly at 900 ℃ while from anthracite coal initially at 600 ℃ and commonly at

430 900 ℃. Similar findings were also reported by Wilks et al. (1993). They all suggest that the improvement of molecular structural in coal observed at relative low PT conditions and at lab time scales was caused by the shear strain that can largely

lower the activation energy for graphitization process of coal (Ross and Bustin, 1990; Ross et al., 1991; Wilks et al., 1993; Bustin et al., 1995a, 1995b). This shear-induced (or strain-induced) graphitization process as a mechanism, from a point view of microstructure, may mainly consist of a) promoting preferred orientation and the rearrangement of aromatic structure systems; b) favoring the motion and modulation of structural defects in order to produce a highly ordered graphite structure (e.g. Beyssac et al., 2002; Wang et al., 2019).

4.2 Mechanisms causing slip weakening

All of our experiments have shown a marked slip weakening behaviour of coal at initial displacement of ~1–2 mm (Fig. 3), i.e. friction coefficient decreased from a peak value approaching ~0.5 to a near steady state value around only 0.3. Similar slip weakening behaviour was also observed on simulated coal-shale gouges when coal content ≥50 vol% under similar experimental conditions (Liu et al., submitted). Recall that mineral content in our coal samples is ~5 % only. This all suggests the presence of minerals should play little role in controlling this significant slip-weakening behaviour. Moreover, the temperature and sliding rates employed in our experiments, together with our XRD results, mean that lubrication effects (Di Toro et al., 2011) due to sample-scale frictional heating and graphitization effects widely seen in high-velocity friction experiments (e.g. Oohashi et al., 2011) can be eliminated. In addition, this marked slip-weakening behaviour was observed in both samples under vacuum dry and samples exposed to DI water at 15 MPa. This suggests that local overpressure effects of DI pore water as a mechanism (e.g. Faulkner et al., 2018) can be eliminated. On the other hand, our microstructure observations on the deformed gouges shown in Fig. 6 and 7 indicate the development of R-, B-, Y- shear bands. Following Logan et al. (1992), strain localization in shear bands may be one of mechanisms responsible for this slip-weakening behaviour of coal. Importantly, our XRD and Raman analysis on the PSZ of the sheared samples suggest the crystallinity was improved in the shear bands upon strain localization associated with strain energy (also see Sect.4.1). As reported by Oohashi et al. (2011), the peak and steady-state friction of amorphous carbon at low slip rates yields ~0.5 while graphite yields ~0.1, suggesting molecular structure of carbon may play a significant role in controlling frictional properties. Recall that our XRD showed that no graphite was formed after friction experiments. We therefore infer the improvement of crystallinity in coal may dominate the steady-state friction of coal approaching ~0.3, which lies in between the steady-state friction of amorphous carbon and graphite. As a result, this all suggests that the marked slip-weakening behaviour of coal could largely be attributed to both the development of R-, B- and Y- shear bands and an increase in crystallinity of coal in the shear bands upon strain localization. However, we also note that little amounts of gas (e.g. CO and/or CH_4) might be produced, in potential, upon volatilization of small molecules and slight breaking of aliphatic chains during shear deformation. It still yet remains unknown whether this process occurred in our experiments and how this process would influence the slip-weakening behaviour.

4.3 Velocity dependence of friction

Our velocity stepping (VS) experiments, from an RSF point view, indicate sliding velocity and pore fluids play roles in rate dependence of friction of coal (see Fig. 4b). In attempt to better illustrate these effects, we plot the (*a-b*) values obtained from the experiments S2–S7 against up-step sliding velocity shown in Fig. 12. Careful inspection of Fig. 12 shows a clear, systematic tendency for a transition from velocity strengthening to velocity weakening, regardless of the experimental conditions employed in this study. Interestingly, the transition occurs at a slip rate of ~10 μm s^{-1} in samples S3–S7 exposed to DI water at 15 MPa, but may occur at a slip rate of ~1 μm s^{-1} in the sample S2 under vacuum dry condition. As this transition from velocity strengthening to velocity weakening is seen both in vacuum dry samples and in samples exposed to pore water at 15 MPa, we infer that the local fluid overpressure effects (e.g. Faulkner et al., 2018) may play little or minor role. On the other hand, we note that, unlike mineral gouges, coal exhibits marked stress-strain-sorption behaviour when exposed to water or/and gas (Liu et al., 2016, 2018). This behaviour leads to swelling/shrinkage strains that strongly depend on chemical activity (pressure) of the adsorbing fluid as well as on the Terzaghi effective stress supported by the solid grain framework. Such effects could conceivably result in competition between compaction and dilatation during shearing of coal gouge, leading to a complex rate-dependence of friction similar to that produced by competition between dilatant granular flow and compaction by pressure solution seen in mineral gouges (Niemeijer and Spiers, 2007; Chen and Spiers, 2016). In the following, we attempt to determine whether the above mechanism proposed by Chen, Niemeijer and Spiers can logically explain the observed transitions.

We first focus on the coal sample under vacuum dry condition, in which the transition from velocity strengthening to weakening occurred at a sliding velocity of ~1 μm s^{-1}. This, following Niemeijer and Spiers (2007), suggests that for the vacuum dry coal, the rate of compaction was similar to the dilatation rate during shear deformation at the imposed sliding velocities of ~1–100 μm s^{-1}. This may be reasonable, because our XRD results as well as the experimental results reported by the literatures (Ross and Bustin, 1990; Ross et al., 1991) suggest that shear deformation (strain) changes the coal molecular structure so that stacks of aromatic layers become more uniformly packed, thus enhancing the rate of compaction to the same order as the rate of the dilatation process at sliding velocities >~1 μm s^{-1}. By contrast, compared to vacuum dry coal, the presence of water may largely increase the compaction rate, by 1–2 orders, because pore water may activate or enhance a) permanent time-dependent compaction (creep) seen in the oedometer-type uniaxial compaction experiments, b) the thermodynamic effect of a stress-driven reduction in water sorption capacity and associated compaction, and c) stress-driven closure of transport paths within the coal particle (Liu et al., 2018). In this case, enhanced compaction rates in the wet coal samples compared to vacuum dry samples may dominate the competition against dilation at sliding velocities of ~1–10 μm s^{-1}, thus promoting velocity strengthening. As a result, our present study suggests the microphysical model developed by Chen, Niemeijer and Spiers (Niemeijer and Spiers, 2007; Chen and Spiers, 2016) may logically explain the observed rate dependence of friction. However, other mechanisms cannot be completely eliminated. More research is needed for a better

495   understanding of such behaviour, for example experiments employing a broader range of slip rates, or investigation of the effects of the compaction rate of coal exposed to different pore fluids.

In addition, we note, from our previous direct shear experiments performed on simulated coal-shale fault gouges under similar PT conditions (see Liu et al., submitted), that the 50:50 volume fraction coal-shale mixtures exhibited a tendency for

500   a transition from velocity weakening to velocity strengthening at a sliding velocity of ~10 μm s^{-1}, as opposed to pure coal samples reported here. This strongly suggests that the presence of mineral phases may play a significant role in rate-dependence of friction of coal-rich faults.

4.4 Implications for frictional strength and seismic potential of coal-rich faults

Our experiments demonstrate that bituminous coal exhibits significant slip-weakening at an initial displacement of ~1–2 mm,

505   when a sliding velocity of 1 μm s^{-1} is imposed under both dry and wet conditions, at a temperature of 100 °C and effective normal stress of 25–45 MPa. Post-test analysis suggests this marked slip-weakening was caused by the development of strain localization in shear bands, accompanied by the improvement of the organization of molecular structure and accordingly of coal maturity. Similar slip weakening behaviour associated with coal-rich shear bands was also observed on simulated coal-shale gouges when coal content ≥ 50 vol%, under similar PT conditions at sliding velocities of 0.1–100 μm s^{-1} (Liu et al.,

510   submitted). This suggests that this marked slip weakening of coal may play a role in promoting unstable slip of coal or coal-rich faults, i.e. facilitating accelerating fault slip and earthquake nucleation in coal-rich fault segments, given appropriately low stiffness of the surrounding rock volume. However, the shear-unload-reshear experiments performed by Liu et al. (submitted) on 50:50 volume fraction coal-shale mixtures suggest that significant slip-weakening occurs only in previously unsheared material in which coal rich shear bands have yet to develop (Logan et al., 1992; Marone, 1998). This suggests that

515   slip-weakening may not be prone to occur on coal-rich faults at the low slip velocities associated with rupture nucleation, as previous tectonic displacements have potentially exceeded the 1–2 mm slip weakening distance observed in our experiments. This is highly uncertain, however, since diagenetic processes in faults during periods of no slip may rework the gouge fabric, so that renewed slip weakening may occur upon reactivation. On the other hand, marked slip-weakening may occur in coal seams when new fractures are produced upon failure of the intact material, caused by underground coal mining or (enhanced)

520   coalbed methane recovery operations. In addition, our SHS experiment shows minor healing (restrengthening) effects of bituminous coal, with transient peak healing in friction increasing with the logarithm of hold time (s) at a linearized rate of only ~0.006. This healing rate would become even smaller when adding 50 vol% shale (see Liu et al. submitted). Post-healing slip weakening effects are correspondingly minor, compared with healing rates typically measured in quartz or carbonate gouges (Nakatani and Scholz, 2004; Chen et al., 2015). We accordingly expect minor or little effect of healing on

525   frictional strength of coal-coal or coal-rich faults, even after geological periods of healing, which again points to very limited scope for slip weakening and seismogenic rupture nucleation in the case of fault reactivation. Besides slip weakening effects, we note that the near steady-state friction strength of coal yields ~0.3, which is insensitive to pore fluids and effective normal

stresses employed in this study. This suggests the mechanical heterogeneity caused by weak coal-coal and coal-smear patches may also play a role in promoting instability of faults (Tembe et al., 2010; Kohli and Zoback, 2013; Buijze et al., 2017; Kaneki and Hirono, 2019).

530

Our VS experiments demonstrate a transition from velocity strengthening to velocity weakening at a slip rate of ~10 μm s⁻¹ for wet coal at 15 MPa pore water pressure, while this occurs at ~1 μm s⁻¹ for vacuum dry coal. We inferred this transition was caused by competition between dilatant granular flow and compaction by stress-strain-sorption behaviour of coal. We

535 note that this rate dependent friction of coal, observed at subseismic slip velocities, may be changed by adding other minerals (e.g. coal-shale mixtures reported by Liu et al., submitted), as the dilatation/compaction processes and accordingly their competition will be changed. Therefore, whether coal-coal or smeared out coal-rich fault patches exhibit slip-weakening behaviour, potentially causing seismogenic rupture nucleation (Scholz, 2019), remains an open question for a given fault.

540 **5 Conclusions**

This paper has investigated frictional properties of simulated bituminous coal gouges under (near) in situ conditions of 100 °C and 25–45 MPa effective normal stresses, employing sliding velocities of 0.1–100 μm s⁻¹. We determined the rate dependence of friction following RSF theory. In addition, frictional healing effects of coal were investigated by performing a single slide-hold-slide experiment with hold durations in the range 300 to 30000 s. Microstructures of the deformed gouges

545 were investigated and the development of molecular structure of coal was analyzed using XRD and Raman spectroscopy. The likely mechanisms controlling the frictional behaviour were then discussed. The main findings are summarized as follows:

1. All simulated coal gouges show marked slip weakening behaviour, from a peak friction coefficient approaching ~0.5 to a near steady state value around only ~0.3, regardless of the applied effective normal stress (25–45 MPa) or

550 the presence of water (at 15 MPa pore pressure) versus vacuum dry conditions.

2. Microstructural observations, performed on the sheared samples using optical microscopy and SEM, show that all coal gouges have developed a principal boundary slip zone with marked stack-layer structure, and a weakly deformed zone. A single sample (S5) shows clear R- and Y- shear bands. This suggests strain localization in the shear bands of coal gouge.

555 3. The crystal structure of the coal samples was investigated using XRD. Our results showed that a) no graphite was formed due to shearing/friction processes; b) following shear deformation, the interlayer spacing of graphite-like structure (d_{002}) decreased from ~3.57 to 3.47–3.53, while the stacked height (L_c) and aromaticity (f_a) increased from ~13 Å to ~20 Å and from 0.44–0.49 to 0.53–0.67, respectively. This suggests an improvement in crystallinity of the

560   sheared coal samples, which may be caused by strain localization associated with strain energy developed in the shear bands.

4. Raman spectroscopy showed that a) D and G bands were present in all samples at ~1360 cm^{-1} and ~1600 cm^{-1}, respectively; b) both D and G bands observed in the sheared samples are more narrow than those observed in the unsheared samples; c) G-FWHM values decreased from 91.3 cm^{-1} to 71.7–79.7 cm^{-1} following shear deformation, while RBS and SI values increased from 227.7 cm^{-1} to 239.3–256.7 cm^{-1} and from 3.27 to 3.65–4.26, respectively.

565   This all indicates an increase of coal maturity, which is in good agreement with our XRD results.

5. On the basis of above findings of 2–4, we suggest that the marked slip-weakening behaviour of coal could largely be attributed to the development of R-, B- and Y- shear bands, i.e. strain localization in shear bands, accompanied by the improvement of crystallinity and maturity of coal.

6. From an RSF point of view, our VS experiments show a transition from velocity strengthening to velocity

570   weakening at slip velocity of ~1 μm s^{-1} in the coal sample under vacuum dry condition, but at ~10 μm s^{-1} in coal samples exposed to DI water at 15 MPa pore pressure. This may be dominated by competition between dilatant granular flow and compaction enhanced by the presence of water.

7. The single SHS experiment revealed transient peak healing (restrengthening) which increased log-linearly with hold time at a rate of ~0.006, demonstrating minor time-dependent healing.

575   8. Our findings, together with our previous research on frictional properties of coal-shale mixtures, suggest that the rather marked slip weakening of coal may not be prone to occur on pre-existing coal-rich faults with a well-developed, localized internal structure, at least for low slip velocities associated with rupture nucleation, but may occur in coal seams when failure or new fractures are produced by underground coal mining or (enhanced) coalbed methane recovery. Such behaviour may lead to accelerating slip and the associated possible seismic hazard. Based

580   on our single SHS experiment, healing is expected to play only a minor role in the frictional strength evolution of coal-rich faults, even for geological time scales, which again points to very limited scope for slip weakening and seismogenic rupture nucleation in the case of fault reactivation. In addition, the rate dependence of friction observed in coal gouges may change due to the addition of other minerals (e.g. coal-shale mixtures), which suggests that the seismogenic potential of coal-bearing faults, via slip-weakening behaviour, remains an open question for a given

585   fault.

Data availability

The landing page for all original data is https://public.yoda.uu.nl/geo/UU01/48I5DA.html, alongside doi:10.24416/UU01-48I5DA.

Author contribution

590 Investigation and research were performed by all of the authors. Specifically, Caiyuan Fan performed XRD and Raman experiments, processed all data and wrote original draft under supervision of Dr. Jinfeng Liu; Jinfeng Liu, with the help of Luuk B. Hunfeld, performed friction experiments and produced metadata; Jinfeng Liu and Prof. Christopher J. Spiers formulated the ideas and research goals of this manuscript; Jinfeng Liu, Luuk B. Hunfeld and Christopher J. Spiers conducted critical review and revisions.

595 **Competing interests**

The authors declare that they have no conflict of interest.

Acknowledgement

This research was funded by the National Natural Science Foundation of China (NSFC project No. 41802230). Dr. Jianye Chen is thanked for discussions and HPT Lab technicians, Gert Kastelein and Floris van Oort, are thanked for their superb
600 technical support. Luuk B. Hunfeld and part of the experimental work conducted at Utrecht were supported through the research program on induced seismicity in the Groningen Gas Field funded by the field operator, the Nederlandse Aardolie Maatschappij (NAM).

References

Ahamed, M. A. A., Perera, M. S. A., Matthai, S. K., Ranjith, P. G. and Dong-yin, L.: Coal composition and structural
605 variation with rank and its influence on the coal-moisture interactions under coal seam temperature conditions – A review article, J. Pet. Sci. Eng., 180, 901–917, doi:10.1016/j.petrol.2019.06.007, 2019.

Aharonov, E. and Scholz, C. H.: A Physics-Based Rock Friction Constitutive Law: Steady State Friction, J. Geophys. Res. Solid Earth, 123(2), 1591–1614, doi:10.1002/2016JB013829, 2018.

Baysal, M., Yürüm, A., Yıldız, B. and Yürüm, Y.: Structure of some western Anatolia coals investigated by FTIR, Raman,
610 13C solid state NMR spectroscopy and X-ray diffraction, Int. J. Coal Geol., 163, 166–176, doi:10.1016/j.coal.2016.07.009, 2016.

Beyssac, O., Rouzaud, J.-N., Goffé, B., Brunet, F. and Chopin, C.: Graphitization in a high-pressure, low-temperature metamorphic gradient: a Raman microspectroscopy and HRTEM study, Contrib. Mineral. Petrol., 143(1), 19–31, doi:10.1007/s00410-001-0324-7, 2002.

615 Beyssac, O., Goffé, B., Petitet, J.-P., Froigneux, E., Moreau, M. and Rouzaud, J.-N.: On the characterization of disordered and heterogeneous carbonaceous materials by Raman spectroscopy, Spectrochim. Acta, Part A, 59(10), 2267–2276, doi:10.1016/S1386-1425(03)00070-2, 2003.

Blanpied, M. L., Tullis, T. E. and Weeks, J. D.: Effects of slip, slip rate, and shear heating on the friction of granite, J. Geophys. Res.: Solid Earth, 103(B1), 489–511, doi:10.1029/97JB02480, 1998.

620 Bonijoly, M., Oberlin, M. and Oberlin, A.: A possible mechanism for natural graphite formation, Int. J. Coal Geol., 1(4), 283–312, doi:10.1016/0166-5162(82)90018-0, 1982.

Brace, W. F. and Byerlee, J. D.: Stick-Slip as a Mechanism for Earthquakes, Science, 153(3739), 990–992, doi:10.1126/science.153.3739.990, 1966.

Buijze, L., Bogert, P. A. J. van den, Wassing, B. B. T., Orlic, B. and Veen, J. ten: Fault reactivation mechanisms and 625 dynamic rupture modelling of depletion-induced seismic events in a Rotliegend gas reservoir, Neth. J. Geosci., 96(5), s131–s148, doi:10.1017/njg.2017.27, 2017.

Buseck, P. R. and Beyssac, O.: From Organic Matter to Graphite: Graphitization, Elements, 10(6), 421–426, doi:10.2113/gselements.10.6.421, 2014.

Buseck, P. R. and Huang, B.-J.: Conversion of carbonaceous material to graphite during metamorphism, Geochim. 630 Cosmochim. Acta, 49(10), 2003–2016, doi:10.1016/0016-7037(85)90059-6, 1985.

Bustin, R. M., Ross, J. V. and Rouzaud, J.-N.: Mechanisms of graphite formation from kerogen: experimental evidence, Int. J. Coal Geol., 28(1), 1–36, doi:10.1016/0166-5162(95)00002-U, 1995a.

Bustin, R. M., Rouzaud, J.-N. and Ross, J. V.: Natural graphitization of anthracite: Experimental considerations, Carbon, 33(5), 679–691, doi:10.1016/0008-6223(94)00155-S, 1995b.

635 Cao, D., Li, X. and Zhang, S.: Influence of tectonic stress on coalification: Stress degradation mechanism and stress polycondensation mechanism, Sci. China, Ser. D: Earth Sci., 50(1), 43–54, doi:10.1007/s11430-007-2023-3, 2007.

Chen, J. and Spiers, C. J.: Rate and state frictional and healing behavior of carbonate fault gouge explained using microphysical model: Microphysical Model for Friction, J. Geophys. Res. Solid Earth, 121(12), 8642–8665, doi:10.1002/2016JB013470, 2016.

640 Chen, J., Verberne, B. A. and Spiers, C. J.: Effects of healing on the seismogenic potential of carbonate fault rocks: Experiments on samples from the Longmenshan Fault, Sichuan, China, J. Geophys. Res. Solid Earth, 120(8), 5479–5506, doi:10.1002/2015JB012051, 2015.

Childres, I., Jauregui, L. A., Park, W., Cao, H. and Chen, Y. P.: Raman spectroscopy of graphene and related materials, in New Developments in Photon and Materials Research, pp. 403–418, Nova Science Publishers, Inc., 2013.

645 Di Toro, G., Han, R., Hirose, T., De Paola, N., Nielsen, S., Mizoguchi, K., Ferri, F., Cocco, M. and Shimamoto, T.: Fault lubrication during earthquakes, Nature, 471(7339), 494–498, doi:10.1038/nature09838, 2011.

Dieterich, J. H.: Modeling of rock friction: 1. Experimental results and constitutive equations, J. Geophys. Res., 84(B5), 2161, doi:10.1029/JB084iB05p02161, 1979.

Dun, W., Guijian, L., Ruoyu, S. and Xiang, F.: Investigation of structural characteristics of thermally metamorphosed coal
650   by FTIR spectroscopy and X-ray diffraction, Energy Fuels, 27(10), 5823–5830, doi:10.1021/ef401276h, 2013.

Ellsworth, W. L.: Injection-Induced Earthquakes, Science, 341(6142), 142-+, doi:10.1126/science.1225942, 2013.

Faulkner, D. R., Sanchez-Roa, C., Boulton, C. and Hartog, S. A. M. den: Pore Fluid Pressure Development in Compacting
Fault Gouge in Theory, Experiments, and Nature, J. Geophys. Res. Solid Earth, 123(1), 226–241,
doi:10.1002/2017JB015130, 2018.

655   Fondriest, M., Smith, S. A. F., Candela, T., Nielsen, S. B., Mair, K. and Toro, G. D.: Mirror-like faults and power dissipation
during earthquakes, Geology, 41(11), 1175–1178, doi:10.1130/G34641.1, 2013.

Hadizadeh, J., Tullis, T. E., White, J. C. and Konkachbaev, A. I.: Shear localization, velocity weakening behavior, and
development of cataclastic foliation in experimental granite gouge, J. Struct. Geol., 71, 86–99, doi:10.1016/j.jsg.2014.10.013,
2015.

660   Henry, D. G., Jarvis, I., Gillmore, G., Stephenson, M. and Emmings, J. F.: Assessing low-maturity organic matter in shales
using Raman spectroscopy: Effects of sample preparation and operating procedure, Int. J. Coal Geol., 191, 135–151,
doi:10.1016/j.coal.2018.03.005, 2018.

Henry, D. G., Jarvis, I., Gillmore, G. and Stephenson, M.: A rapid method for determining organic matter maturity using
Raman spectroscopy: Application to Carboniferous organic-rich mudstones and coals, Int. J. Coal Geol., 203, 87–98,
665   doi:10.1016/j.coal.2019.01.003, 2019a.

Henry, D. G., Jarvis, I., Gillmore, G. and Stephenson, M.: Raman spectroscopy as a tool to determine the thermal maturity of
organic matter: Application to sedimentary, metamorphic and structural geology, Earth-Sci. Rev., 198, 102936,
doi:10.1016/j.earscirev.2019.102936, 2019b.

Hirsch, P.: X-ray scattering from coals, Proc. R. Soc. A, 226(1165), 29, doi:doi.org/10.1098/rspa.1954.0245, 1954.

670   Hol, S., Peach, C. J. and Spiers, C. J.: Applied stress reduces the CO2 sorption capacity of coal, Int. J. Coal Geol., 85(1),
128–142, doi:10.1016/j.coal.2010.10.010, 2011.

Hou, Q., Luo, Y., Han, Y., Du, J. and Xu, R.: Gas generation during middle-rank coal deformation and the reliminary
discussion ofthe mechanism, J. China Coal Soc., 39(8), 1678-1682 (in Chinese), 2014.

Hou, Q., Han, Y., Wang, J., Dong, Y. and Pan, J.: The impacts of stress on the chemical structure of coals: a mini-review
675   based on the recent development of mechanochemistry, Science Bulletin, 62(13), 965–970, doi:10.1016/j.scib.2017.06.004,
2017.

Hunfeld, L. B., Niemeijer, A. R. and Spiers, C. J.: Frictional Properties of Simulated Fault Gouges from the Seismogenic
Groningen Gas Field Under In Situ P-T Chemical Conditions: Friction of Groningen fault gouges, J. Geophys. Res. Solid
Earth, 122(11), 8969–8989, doi:10.1002/2017JB014876, 2017.

680   Ikari, M. J., Saffer, D. M. and Marone, C.: Frictional and hydrologic properties of a major splay fault system, Nankai
subduction zone, Geophys. Res. Lett., 36(20), doi:10.1029/2009GL040009, 2009.

Ju, Y., Jiang, B., Hou, Q. and Wang, G.: Relationship between nanoscale deformation of coal structure and metamorphic-deformed environments, Chin. Sci. Bull., 50(16), 1785–1796, doi:10.1360/04wd0205, 2005.

Kaneki, S. and Hirono, T.: Diagenetic and shear-induced transitions of frictional strength of carbon-bearing faults and their

685 implications for earthquake rupture dynamics in subduction zones, Sci. Rep., 9(1), 7884, doi:10.1038/s41598-019-44307-y, 2019.

Kaneki, S., Ichiba, T. and Hirono, T.: Mechanochemical Effect on Maturation of Carbonaceous Material: Implications for Thermal Maturity as a Proxy for Temperature in Estimation of Coseismic Slip Parameters, Geophys. Res. Lett., 45(5), 2248–2256, doi:10.1002/2017GL076791, 2018.

690 Khatibi, S., Ostadhassan, M., Tuschel, D., Gentzis, T., Bubach, B. and Carvajal-Ortiz, H.: Raman spectroscopy to study thermal maturity and elastic modulus of kerogen, Int. J. Coal Geol., 185, 103–118, doi:10.1016/j.coal.2017.11.008, 2018.

Kirilova, M., Toy, V. G., Timms, N., Halfpenny, A., Menzies, C., Craw, D., Beyssac, O., Sutherland, R., Townend, J., Boulton, C., Carpenter, B. M., Cooper, A., Grieve, J., Little, T., Morales, L., Morgan, C., Mori, H., Sauer, K. M., Schleicher, A. M., Williams, J. and Craw, L.: Textural changes of graphitic carbon by tectonic and hydrothermal processes in an active

695 plate boundary fault zone, Alpine Fault, New Zealand, Geological Society, London, Special Publications, 453(1), 205–223, doi:10.1144/SP453.13, 2017.

Kohli, A. H. and Zoback, M. D.: Frictional properties of shale reservoir rocks, J. Geophys. Res. Solid Earth, 118(9), 5109–5125, doi:10.1002/jgrb.50346, 2013.

Kuo, L.-W., Li, H., Smith, S. A. F., Di Toro, G., Suppe, J., Song, S.-R., Nielsen, S., Sheu, H.-S. and Si, J.: Gouge

700 graphitization and dynamic fault weakening during the 2008 Mw 7.9 Wenchuan earthquake, Geology, 42(1), 47–50, doi:10.1130/G34862.1, 2014.

Li, K., Khanna, R., Zhang, J., Barati, M., Liu, Z., Xu, T., Yang, T. and Sahajwalla, V.: Comprehensive Investigation of Various Structural Features of Bituminous Coals Using Advanced Analytical Techniques, Energy Fuels, 29(11), 7178–7189, doi:10.1021/acs.energyfuels.5b02064, 2015a.

705 Li, Z., Wei, X.-Y., Yan, H.-L. and Zong, Z.-M.: Insight into the structural features of Zhaotong lignite using multiple techniques, Fuel, 153, 176–182, doi:10.1016/j.fuel.2015.02.117, 2015b.

Liu, J., Hunfeld, L. B., Niemeijer, A. and Spiers, C. J.: Frictional properties of simulated shale-coal fault gouges: Implications for induced seismicity in source rocks below Europe's largest gas field, submitted to Int. J. Coal Geol..

Liu, J. and Hunfeld, L. B.: Frictional slip weakening and shear-enhanced crystallinity in simulated coal fault gouges at

710 subseismic slip rates, EPOS repository, v1, doi:10.24416/UU01-48I5DA, 2020.

Liu, J., Spiers, C. J., Peach, C. J. and Vidal-Gilbert, S.: Effect of lithostatic stress on methane sorption by coal: Theory vs. experiment and implications for predicting in situ coalbed methane content, Int. J. Coal Geol., 167, 48–64, doi:10.1016/j.coal.2016.07.012, 2016.

Liu, J., Fokker, P. A., Peach, C. J. and Spiers, C. J.: Applied stress reduces swelling of coal induced by adsorption of water,

715 Geomechanics for Energy and the Environment, 16, 45–63, doi:10.1016/j.gete.2018.05.002, 2018.

Logan, J. M., Dengo, C. A., Higgs, N. G. and Wang, Z. Z.: Fabrics of Experimental Fault Zones: Their Development and Relationship to Mechanical Behavior, in International Geophysics, vol. 51, edited by B. Evans and T. Wong, pp. 33–67, Academic Press, Lodon., 1992.

Lu, L., Sahajwalla, V., Kong, C. and Harris, D.: Quantitative X-ray diffraction analysis and its application to various coals, Carbon, 39(12), 1821–1833, doi:10.1016/S0008-6223(00)00318-3, 2001.

Ma, T.-B., Wang, L.-F., Hu, Y.-Z., Li, X. and Wang, H.: A shear localization mechanism for lubricity of amorphous carbon materials, Sci. Rep., 4, 3662, 2014.

Marone, C.: Laboratory-derived Friction Laws and their Application to Seismic Faulting, Annu. Rev. Earth Planet. Sci., 26(1), 643–696, doi:10.1146/annurev.earth.26.1.643, 1998.

Mathews, J. P. and Chaffee, A. L.: The molecular representations of coal – A review, Fuel, 96, 1–14, doi:10.1016/j.fuel.2011.11.025, 2012.

Nakatani, M. and Scholz, C. H.: Frictional healing of quartz gouge under hydrothermal conditions: 1. Experimental evidence for solution transfer healing mechanism, J. Geophys. Res. Solid Earth, 109(B7), doi:10.1029/2001JB001522, 2004.

Niemeijer, A. R. and Spiers, C. J.: A microphysical model for strong velocity weakening in phyllosilicate-bearing fault gouges, J. Geophys. Res., 112(B10), B10405, doi:10.1029/2007JB005008, 2007.

Niu, Z., Liu, G., Yin, H., Wu, D. and Zhou, C.: Investigation of mechanism and kinetics of non-isothermal low temperature pyrolysis of perhydrous bituminous coal by in situ FTIR, Fuel, 172, 1–10, doi:10.1016/j.fuel.2016.01.007, 2016.

Oberlin, A.: Carbonization and graphitization, Carbon, 22(6), 521–541, doi:10.1016/0008-6223(84)90086-1, 1984.

Okolo, G. N., Neomagus, H. W. J. P., Everson, R. C., Roberts, M. J., Bunt, J. R., Sakurovs, R. and Mathews, J. P.: Chemical–structural properties of South African bituminous coals: Insights from wide angle XRD–carbon fraction analysis, ATR–FTIR, solid state 13C NMR, and HRTEM techniques, Fuel, 158, 779–792, doi:10.1016/j.fuel.2015.06.027, 2015.

Oohashi, K., Hirose, T. and Shimamoto, T.: Shear-induced graphitization of carbonaceous materials during seismic fault motion: Experiments and possible implications for fault mechanics, J. Struct. Geol., 33(6), 1122–1134, doi:10.1016/j.jsg.2011.01.007, 2011.

Oohashi, K., Hirose, T., Kobayashi, K. and Shimamoto, T.: The occurrence of graphite-bearing fault rocks in the 4fault system, Japan: Origins and implications for fault creep, J. Struct. Geol., 38, 39–50, doi:10.1016/j.jsg.2011.10.011, 2012.

Oohashi, K., Hirose, T. and Shimamoto, T.: Graphite as a lubricating agent in fault zones: An insight from low- to high-velocity friction experiments on a mixed graphite-quartz gouge, J. Geophys. Res. Solid Earth, 118(5), 2067–2084, doi:10.1002/jgrb.50175, 2013.

Öztaş, N. A. and Yürüm, Y.: Pyrolysis of Turkish Zonguldak bituminous coal. Part 1. Effect of mineral matter, Fuel, 79(10), 1221–1227, doi:10.1016/S0016-2361(99)00255-0, 2000.

Pan, J., Lv, M., Bai, H., Hou, Q., Li, M. and Wang, Z.: Effects of Metamorphism and Deformation on the Coal Macromolecular Structure by Laser Raman Spectroscopy, Energy Fuels, 31(2), 1136–1146, doi:10.1021/acs.energyfuels.6b02176, 2017.

750   Potgieter-Vermaak, S., Maledi, N., Wagner, N., Van Heerden, J. H. P., Van Grieken, R. and Potgieter, J. H.: Raman spectroscopy for the analysis of coal: a review, J. Raman Spectrosc., 42(2), 123–129, doi:10.1002/jrs.2636, 2011.

Rice, J. R.: Heating and weakening of faults during earthquake slip, J. Geophys. Res. Solid Earth, 111(B5), n/a-n/a, doi:10.1029/2005JB004006, 2006.

Ross, J. V. and Bustin, R. M.: The role of strain energy in creep graphitization of anthracite, Nature, 343(6253), 58–60,
755   doi:10.1038/343058a0, 1990.

Ross, J. V., Bustin, R. M. and Rouzaud, J. N.: Graphitization of high rank coals—the role of shear strain: experimental considerations, Org. Geochem., 17(5), 585–596, doi:10.1016/0146-6380(91)90002-2, 1991.

Ruina, A.: Slip instability and state variable friction laws, J. Geophys. Res. Solid Earth, 88(B12), 10359–10370, doi:10.1029/JB088iB12p10359, 1983.

760   Sadezky, A., Muckenhuber, H., Grothe, H., Niessner, R. and Pöschl, U.: Raman microspectroscopy of soot and related carbonaceous materials: Spectral analysis and structural information, Carbon, 43(8), 1731–1742, doi:10.1016/j.carbon.2005.02.018, 2005.

Samuelson, J. and Spiers, C. J.: Fault friction and slip stability not affected by Co2 storage: Evidence from short-term laboratory experiments on North Sea reservoir sandstones and caprocks, Int. J. Greenhouse Gas Control, 11, S78–S90,
765   doi:10.1016/j.ijggc.2012.09.018, 2012.

Schito, A., Romano, C., Corrado, S., Grigo, D. and Poe, B.: Diagenetic thermal evolution of organic matter by Raman spectroscopy, Org. Geochem., 106, 57–67, doi:10.1016/j.orggeochem.2016.12.006, 2017.

Scholz, C. H.: Earthquakes and friction laws, Nature, 391, 37–42, 1998.

Scholz, C. H.: The Mechanics of Earthquakes and Faulting, 3rd ed., Cambridge University Press., 2019.

770   Siman-Tov, S., Aharonov, E., Sagy, A. and Emmanuel, S.: Nanograins form carbonate fault mirrors, Geology, 41(6), 703–706, doi:10.1130/G34087.1, 2013.

Song, Y., Jiang, B. and Han, Y.: Macromolecular response to tectonic deformation in low-rank tectonically deformed coals (TDCs), Fuel, 219, 279–287, doi:10.1016/j.fuel.2018.01.133, 2018.

Song, Y., Jiang, B. and Qu, M.: Macromolecular evolution and structural defects in tectonically deformed coals, Fuel, 236,
775   1432–1445, doi:10.1016/j.fuel.2018.09.080, 2019.

Tembe, S., Lockner, D. A. and Wong, T.-F.: Effect of clay content and mineralogy on frictional sliding behavior of simulated gouges: Binary and ternary mixtures of quartz, illite, and montmorillonite, J. Geophys. Res. Solid Earth, 115(B3), doi:10.1029/2009JB006383, 2010.

Tuinstra, F. and Koenig, J. L.: Raman spectrum of graphite, J. Chem. Phys., 53(3), 1126–30, doi:10.1063/1.1674108, 1970.

780   Ulyanova, E. V., Molchanov, A. N., Prokhorov, I. Y. and Grinyov, V. G.: Fine structure of Raman spectra in coals of different rank, Int. J. Coal Geol., 121, 37–43, doi:10.1016/j.coal.2013.10.014, 2014.

Verberne, B. A., Bresser, J. H. P. de, Niemeijer, A. R., Spiers, C. J., Winter, D. A. M. de and Plümper, O.: Nanocrystalline slip zones in calcite fault gouge show intense crystallographic preferred orientation: Crystal plasticity at sub-seismic slip rates at 18–150 °C, Geology, 41(8), 863–866, doi:10.1130/G34279.1, 2013.

785 Verberne, B. A., Spiers, C. J., Niemeijer, A. R., De Bresser, J. H. P., De Winter, D. A. M. and Plümper, O.: Frictional Properties and Microstructure of Calcite-Rich Fault Gouges Sheared at Sub-Seismic Sliding Velocities, Pure Appl. Geophys., 171(10), 2617–2640, doi:10.1007/s00024-013-0760-0, 2014a.

Verberne, B. A., Plumper, O., de Winter, D. A. M. and Spiers, C. J.: Superplastic nanofibrous slip zones control seismogenic fault friction, Science, 346(6215), 1342–1344, doi:10.1126/science.1259003, 2014b.

790 Wang, L., Cao, D., Peng, Y., Ding, Z. and Li, Y.: Strain-induced graphitization mechanism of coal-based graphite from lutang, hunan province, china, Minerals, 9(10), doi:10.3390/min9100617, 2019.

Westbrook, G. K., Kusznir, N. J., Browitt, C. W. A. and Holdsworth, B. K.: Seismicity induced by coal mining in Stoke-on-Trent (U.K.), Eng. Geol., 16(3), 225–241, doi:10.1016/0013-7952(80)90017-4, 1980.

Wilkins, R. W. T., Boudou, R., Sherwood, N. and Xiao, X.: Thermal maturity evaluation from inertinites by Raman 795 spectroscopy: The 'RaMM' technique, Int. J. Coal Geol., 128–129, 143–152, doi:10.1016/j.coal.2014.03.006, 2014.

Wilks, K. R., Mastalerz, M., Bustin, R. M. and Ross, J. V.: The role of shear strain in the graphitization of a high-volatile bituminous and an anthracitic coal, Int. J. Coal Geol., 22(3–4), 247–277, doi:10.1016/0166-5162(93)90029-A, 1993.

Xu, R., Li, H., Guo, C. and Hou, Q.: The mechanisms of gas generation during coal deformation: Preliminary observations, Fuel, 117, 326–330, doi:10.1016/j.fuel.2013.09.035, 2014.

800 Yen, T. Fu., Erdman, J. G. and Pollack, S. S.: Investigation of the Structure of Petroleum Asphaltenes by X-Ray Diffraction, Anal. Chem., 33(11), 1587–1594, doi:10.1021/ac60179a039, 1961.

Zhang, W., Chen, S., Han, F. and Wu, D.: An experimental study on the evolution of aggregate structure in coals of different ranks by in situ X-ray diffractometry, Anal. Methods, 7(20), 8720–8726, doi:10.1039/C5AY01922B, 2015.

Zhang, Y. and Li, Z.: Raman spectroscopic study of chemical structure and thermal maturity of vitrinite from a suite of 805 Australia coals, Fuel, 241, 188–198, doi:10.1016/j.fuel.2018.12.037, 2019.

Zhao, L., Guo, H. and Ma, Q.: Study on gaseous products distributions during coal pyrolysis, Coal Conversion, 30(1), 5-9 (in Chinese), 2007.

Table 1. List of experiments, experimental conditions and key mechanical data. VS = velocity stepping, SHS = slide-hold-slide. Note that all experiments reported here were performed at ~100 °C. μ_{peak} represents the peak friction coefficient obtained at 0.5–0.75 mm shear displacement, μ_{ss1} and μ_{ss2} represent the near steady-state friction coefficient obtained at ~2.2 mm and ~5.7 mm shear displacement respectively. D_{tot} represents the total shear displacement. t_0 and t represent the thickness of the gouge layer measured before and after the experiments, respectively. τ_{ss2} and ε represent the steady-state shear stress and shear strain measured at the shear displacement of ~5.7 mm and the latter equals to 5.7 divided by initial thickness t_0.

Exp./ Sam.	σ_n [MPa]	P_f [MPa]	μ_{peak} [-]	μ_{ss1} [-]	μ_{ss2} [-]	D_{tot} [mm]	V [µm s^{-1}]	t_0 [mm]	t [mm]	τ_{ss2} [MPa]	ε [-]

S*	*	*								
S0	20	*								
VS										
S1	40	0	0.494	0.327	0.295	6.201	0.1–100	1.03	0.93	11.73	5.56
S2	40	0	0.465	0.278	0.244	5.563	0.1–100	0.92	0.75	9.62	6.16
S3	40	15	0.524	0.338	0.282	5.602	0.1–100	1.00	0.75	6.87	5.70
S4	50	15	N/A	0.279	0.253	6.183	0.1–100	1.18	0.83	8.78	4.85
S5	55	15	0.441	0.258	0.228	5.766	0.1–100	0.90	0.65	8.91	6.33
S6	55	15	0.485	0.293	0.256	6.010	0.1–100	0.90	0.73	10.14	6.33
S7	60	15	0.454	0.273	0.245	5.750	0.1–100	1.00	0.80	10.85	5.70
SHS										
S8	55	15	0.460	0.275	0.244	6.057	1	1.00	0.80	9.64	5.70

S* represents the starting, loose coal powders without pre-compaction process.
S0 represents the compacted coal gouge layer only, i.e. without the shear deformation.
S* and S0 are used as the control samples for XRD and Raman tests, in an attempt to determine the effects of shear deformation on molecular structure of carbon in coal.
N/A: This value is missing.

810

Table 2. Summary of RSF data for all velocity-stepping experiments reported in this paper.

Sam./Steps	V_0 [μm s^{-1}]	V [μm s^{-1}]	$a-b$ [-]	a [-]	b [-]	D_c [mm]
S1						
V_step1	0.1	1	N/A	N/A	N/A	N/A
V_step2	1	10	-0.0055	0.0051	0.0094	0.0074
V_step3	10	100	N/A	N/A	N/A	N/A
S2						
V_step1	0.1	1	0.0001	0.0030	0.0029	0.0029
V_step2	1	10	-0.0018	0.0028	0.0047	0.0120
V_step3	10	100	-0.0047	0.0629	0.0676	0.0440
S3						
V_step1	0.1	1	N/A	N/A	N/A	N/A
V_step2	1	10	0.0010	0.0034	0.0024	0.0032
V_step3	10	100	-0.0042	0.0637	0.0679	0.0370
S4						
V_step1	0.1	1	0.0061	0.0128	0.0067	0.0014
V_step2	1	10	0.0012	0.0043	0.0031	0.0101
V_step3	10	100	-0.0012	0.3271	0.3283	0.0578
S5						
V_step1	0.1	1	0.0052	0.0327	0.0276	0.0014
V_step2	1	10	-0.0019	0.0057	0.0076	0.0364
V_step3	10	100	-0.0049	0.1008	0.1057	0.0436

S6						
V_step1	0.1	1	0.0135	0.0470	0.0336	0.0071
V_step2	1	10	0.0009	0.0039	0.0030	0.0134
V_step3	10	100	-0.0008	0.0091	0.0099	0.0234
S7						
V_step1	0.1	1	0.0014	0.0047	0.0033	0.0067
V_step2	1	10	0.0001	0.0029	0.0028	0.0143
V_step3	10	100	-0.0054	0.4209	0.4264	0.0586

N/A: This value cannot be obtained as the fitting quality is low.

Table 3. Coal crystal structure parameters determined from XRD profiles.

	Sam.	$2\theta_{002}$ [°]	$2\theta_{10}$ [°]	β_{002} [°]	β_{10} [°]	d_{002} [Å]	L_c [Å]	L_a [Å]	I_{26}/I_{20}	f_a
	S*	24.81	43.59	5.81	8.94	3.58	14.26	20.22	1.29	0.44
		24.93	43.59	5.48	8.38	±0.01	±0.59	±0.92	±0.10	±0.04
	S0	25.02	43.72	6.10	8.13	3.56	12.87	21.46	1.21	0.49
		24.94	43.80	6.41	8.18	±0.01	±0.45	±0.09	±0.03	±0.03
	S1	25.57	44.73	3.88	11.79	3.48	20.76	14.90	1.72	0.56
	S3	25.25	43.96	5.28	9.13	3.52	15.25	19.18	1.33	0.53
P	S4	25.62	44.17	3.77	11.04	3.47	21.37	15.88	1.76	0.56
S	S5	25.46	44.30	3.92	10.82	3.49	20.22	15.97	2.23	0.67
Z		25.51	44.30	4.05	11.15	±0.00	±0.46	±0.34	±0.00	±0.00
	S7	25.57	44.36	4.06	10.58	3.48	19.84	16.58	1.96	0.61
	S8	25.21	43.82	5.18	9.10	3.53	15.54	19.24	1.69	0.61
	S1	25.22	44.17	4.61	10.96	3.53	17.46	15.99	2.11	0.64
	S3	25.55	43.80	4.51	9.52	3.48	17.86	18.39	1.51	0.51
W	S4	25.34	44.11	4.49	8.97	3.51	17.93	19.54	2.29	0.63
D	S5	25.40	43.97	4.55	10.77	3.50	17.70	16.26	1.58	0.54
Z	S7	25.28	44.21	4.65	7.74	3.52	17.31	22.65	1.98	0.60
	S8	25.54	43.67	4.27	10.27	3.48	18.86	17.04	1.16	0.43

PSZ and WDZ represent principal boundary slip zone and weakly deformed zone retrieved from the sheared samples.
Note that the parameter for Sample S*, S0 and S5 are mean values, associated with standard deviation, obtained from the reproducible tests.

815

Table 4. Parameters obtained from normalized Raman spectra using the method reported by Henry et al. (2018).

Sam.		S*	S4*	S0	S1	S2	S3	S4	S5	S6	S7	S8
D Position	[cm⁻¹]	1368	1354	1369	1359	1364	1361	1362	1361	1352	1348	1347
Stdev		/	10.1	7.0	8.5	1.5	7.5	8.7	2.5	8.4	2.9	3.0

D-FWHM	[cm⁻¹]	N/A	N/A	N/A	209.4	N/A	N/A	N/A	N/A	N/A	217.3	201.3
Stdev		/	N/A	N/A	7.7	N/A	N/A	N/A	N/A	N/A	4.6	10.1
G position	[cm⁻¹]	1601	1601	1597	1603	1601	1601	1602	1601	1603	1601	1604
Stdev		/	0.0	3.5	1.5	0.0	0.0	1.2	0.6	1.7	0.6	0.6
G-FWHM	[cm⁻¹]	84.0	78.0	91.3	73.9	77.7	79.0	79.7	78.0	77.0	77.3	71.7
Stdev		/	4.6	4.5	4.4	0.6	2.6	4.0	1.0	6.3	0.6	3.5
RBS	[cm⁻¹]	233.0	246.7	227.7	244.5	237.3	240.0	239.7	239.3	250.5	252.3	256.7
Stdev		/	10.1	10.3	9.8	1.5	7.5	9.2	3.1	10.1	3.2	3.1
I_D/I_G	/	0.540	0.548	0.543	0.553	0.555	0.561	0.543	0.553	0.553	0.552	0.551
Stdev		/	0.024	0.004	0.009	0.006	0.014	0.006	0.013	0.019	0.011	0.003
SI	/	3.70	3.84	3.27	4.26	3.65	3.78	3.76	3.65	3.75	3.79	4.08
Stdev		/	0.65	0.34	0.32	0.10	0.33	0.09	0.08	0.30	0.10	0.13

S4* represents the weakly deformed zone of sample S4.
N/A: This value cannot be obtained due to the limitations of the processing method described in Sect.2.5.3.
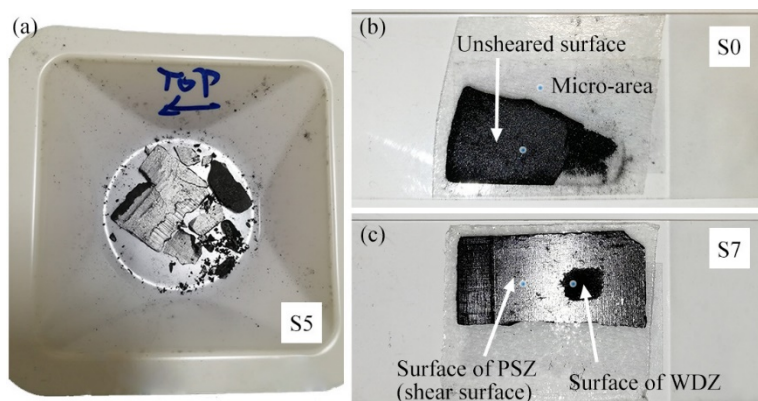
Figure 1: Post treatment of the recovered fragments used for microstructural observation, XRD and Raman spectroscopy. (a) Stored loose fragments. (b) The free surface of the unsheared sample S0 that was glued on a glass slide. (c) The slip surface of the sample S7, showing the surface of principal slip zone (PSZ) and of weakly deformed zone (WDZ).
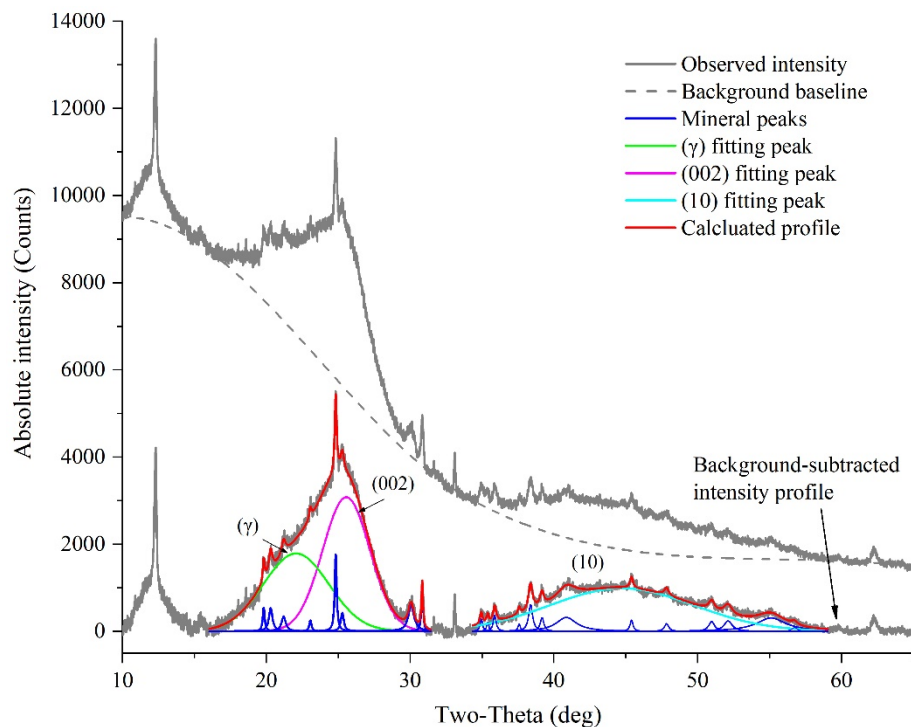
Figure 2: Fitting curves in X-ray diffraction pattern for the sample S1.

825
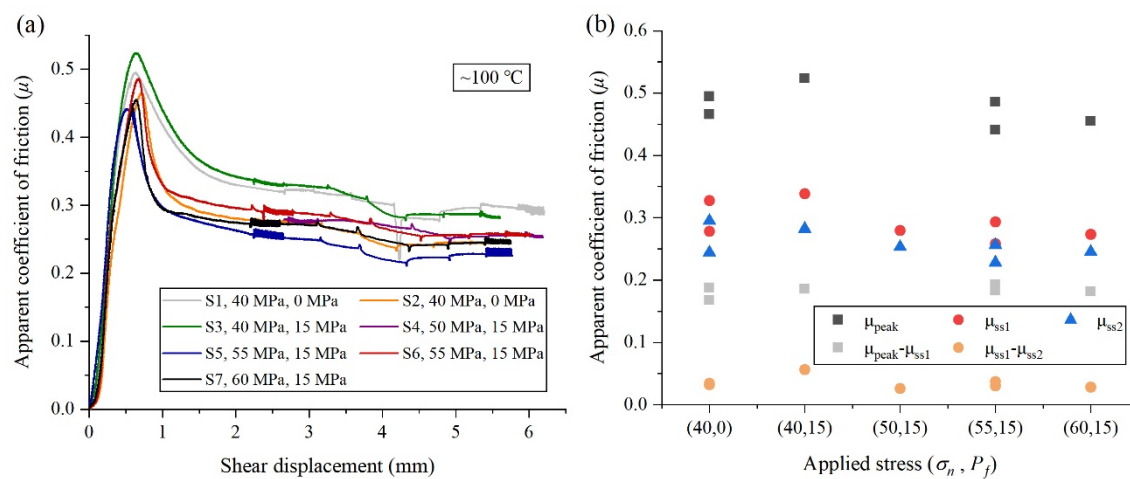
Figure 3: Frictional properties of the samples S1–S7 obtained from the velocity stepping experiments. (a) Apparent coefficient of friction (μ) against shear displacement. (b) Apparent coefficient of friction (μ) against applied stress (σ_n, P_f).
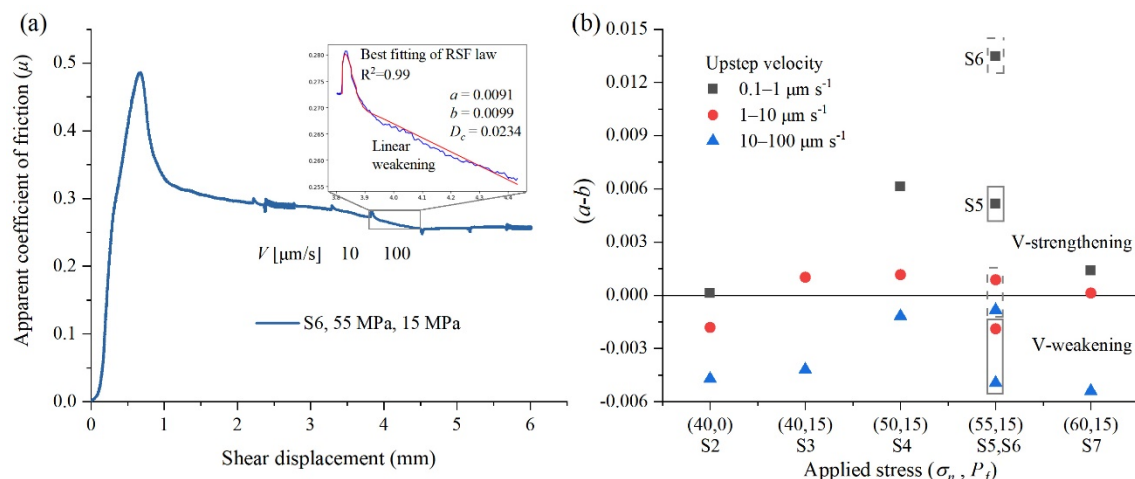
Figure 4: (a) Results of experiment S6, illustrating the best fitting of a full RSF law to the experimental data obtained at velocity step from 10 to 100 μm s⁻¹. (b) (a-b) values, obtained from upward velocity steps using a full RSF fit, versus applied stress (σ_n, P_f).
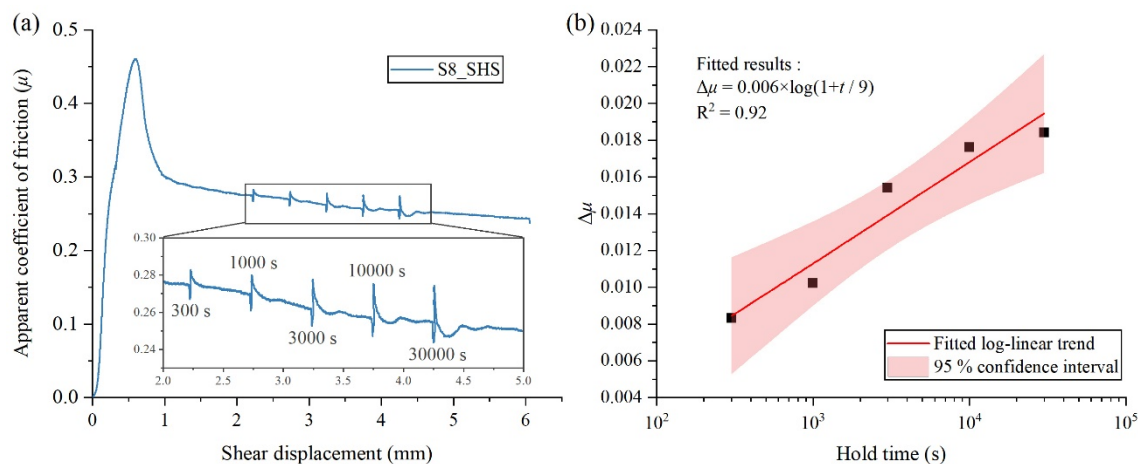
Figure 5: Slide-hold-slide experimental data for sample S8 tested at a pore fluid pressure of 15 MPa and a confining pressure of 55 MPa. (a) Friction coefficient versus shear displacement, showing slide-hold-slide testing sequence. (b) Transient peak healing or post-hold frictional restrengthening plotted as a function of the logarithm of hold time. The black solid squares represent the experimental data derived from (a).

840
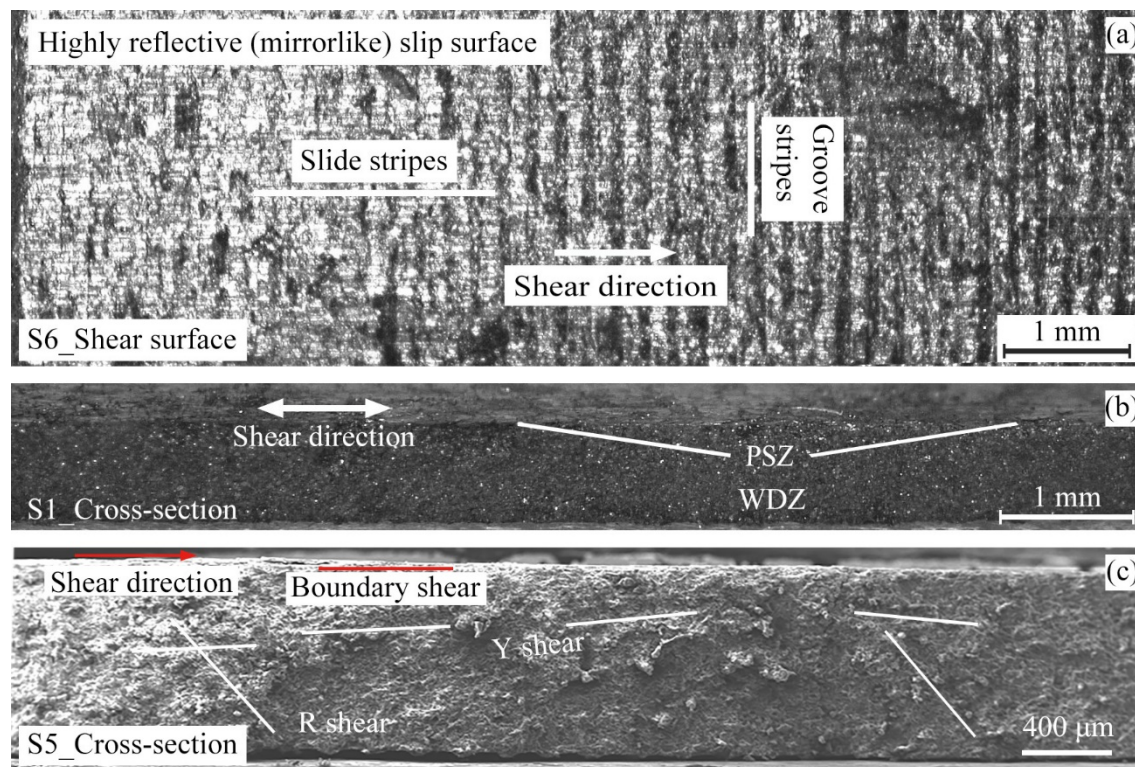
Figure 6: Microstructure of samples S1, S5 and S6 after shear deformation. (a) and (b) were imaged using optical microscope in a reflected light mode, while (c) was imaged using SEM in secondary electron mode. (a) The shear surface of sample S6, showing highly reflective (mirrorlike) slip surface. (b) The cross-section of sample S1 in an orientation parallel to the shear direction, indicating a principal slip zone (PSZ) and a weakly deformed zone (WDZ). (c) The cross-section of sample S5 in an orientation

845 **parallel to the shear direction, showing the development of first R shear, and then boundary and Y shear bands.**
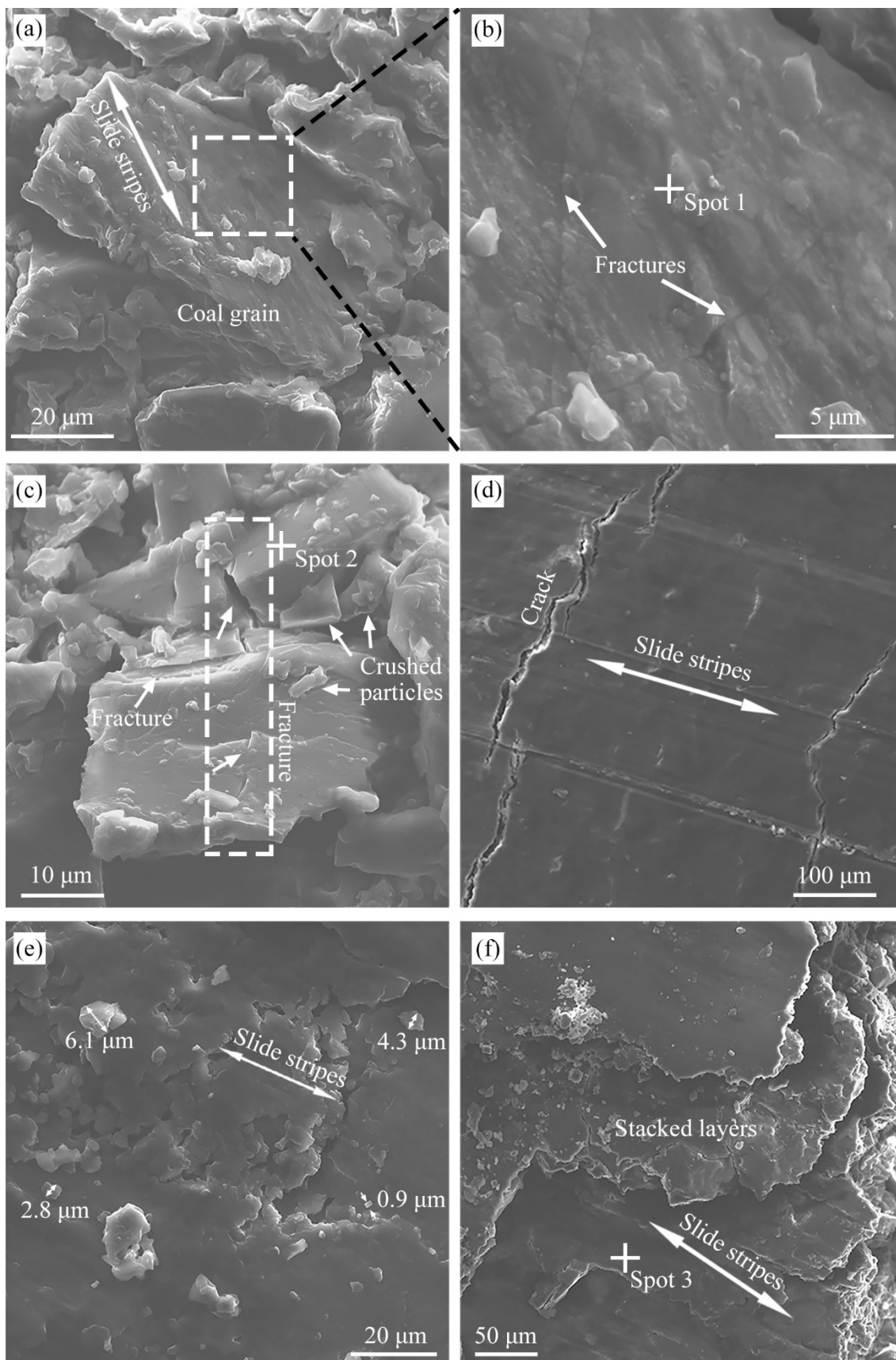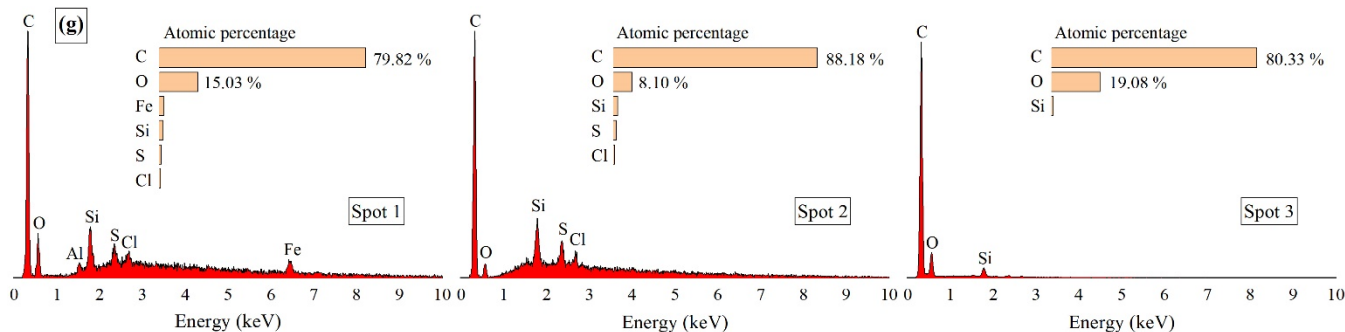
Figure 7: SEM secondary electron images of the samples S4 (a, b, c, f) and S5 (d, e) after direct shear experiments and EDS data (g)
for the representative spots. (a) Randomly oriented coal grain with slide stripes in the WDZ, located in the cross-section of S4. (b)
The fractures inside the coal grain shown in (a). (c) Fractures inside coal grains to form crushed particles. (d) The central region of
shear surface of sample S5, showing cracks and slide stripes. (e) Small coal particles (<~10 μm) in the broken edge of shear surface.
(f) Remarkable layered structure at the margins of slip zone, likely reflecting an interaction between PSZ and WDZ and the role of
PSZ during friction process. (g) EDS data for three spots located in S4, roughly showing the elemental composition.
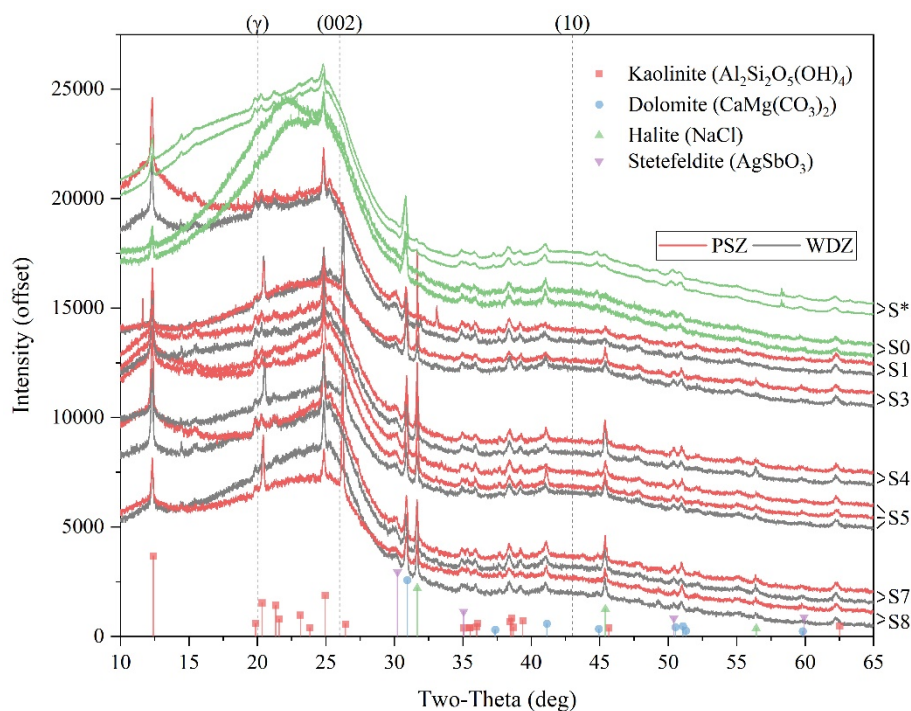
Figure 8: X-ray diffractograms for starting coal powder S*, pre-compacted coal (unsheared) sample S0, and sheared samples S1–
S8 except S2 and S6. The minor peaks are marked by possible minerals using points. The red and black lines represent XRD
profile for samples retrieved from the principal boundary slip zone (PSZ) and the weakly deformed zone (WDZ). Note that the
intensity for sample S* was reduced by ten times to a comparable scale.
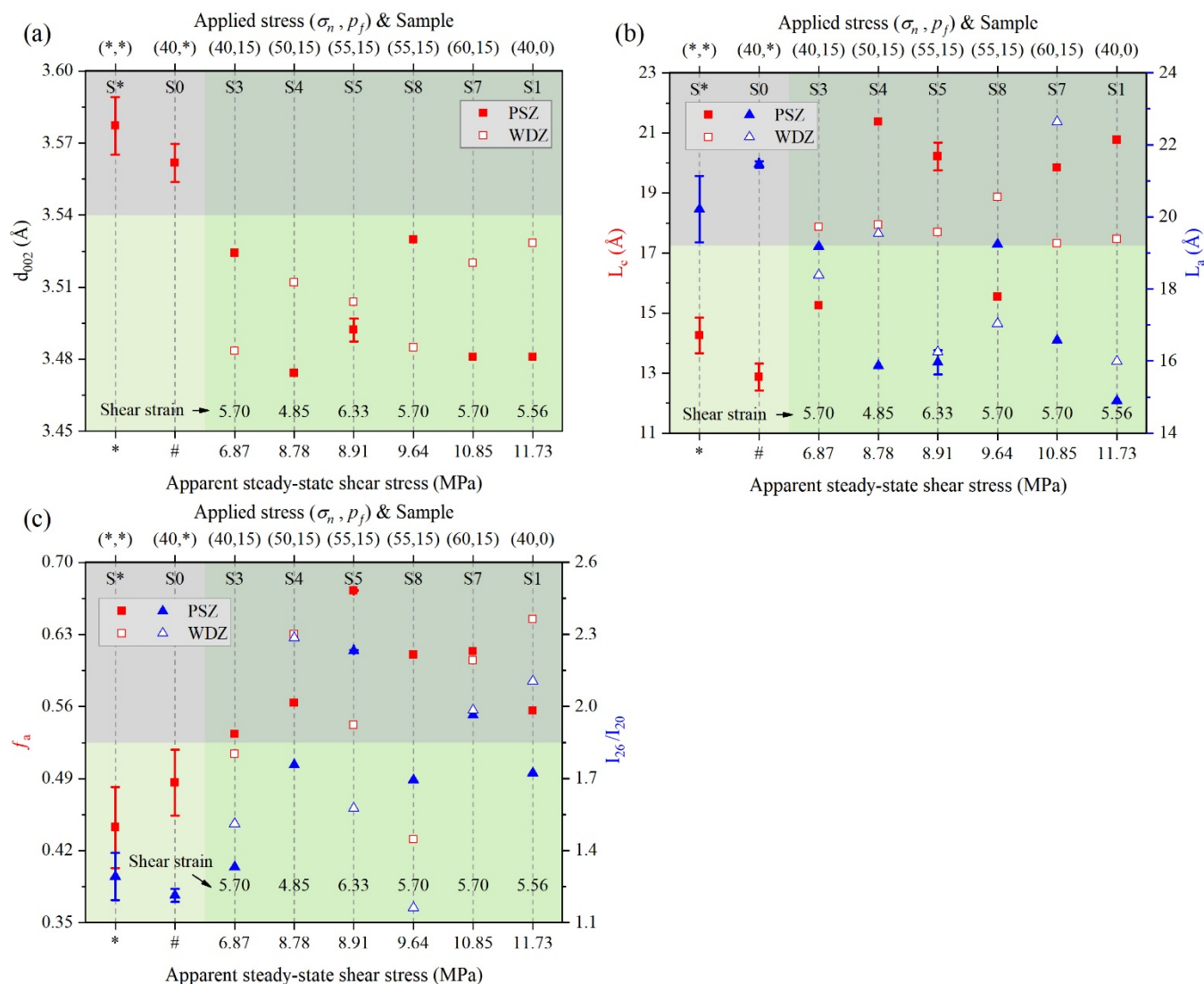
Figure 9: Representative crystal structure parameters obtained from the samples S*–S8 versus apparent steady-state shear stress associated with shear strain measured at shear displacement of ~5.7 mm in the direct shear experiments. Note that * and # represent coal powder S* and the pre-compacted sample S0 without shearing. Note that solid and hollow squares or triangles represent the values for the PSZ and WDZ retrieved from the sheared samples, respectively. The error bars for samples S*, S0 and S5 are the standard deviations.
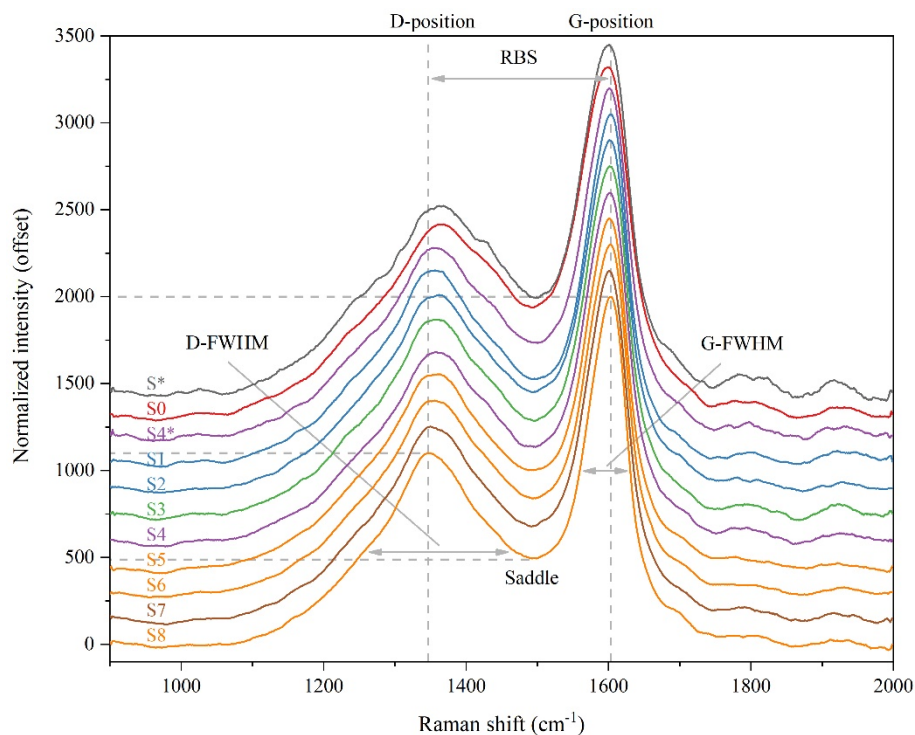
870 **Figure 10: The processed Raman spectra of coal samples, showing the spectra differences between unsheared samples (S* and S0) and sheared samples (S1–S8). Note that different colors mean different experimental conditions and S4* represents the weakly deformed zone of the sample S4. Some important parameters were marked according to Henry et al. (2018).**
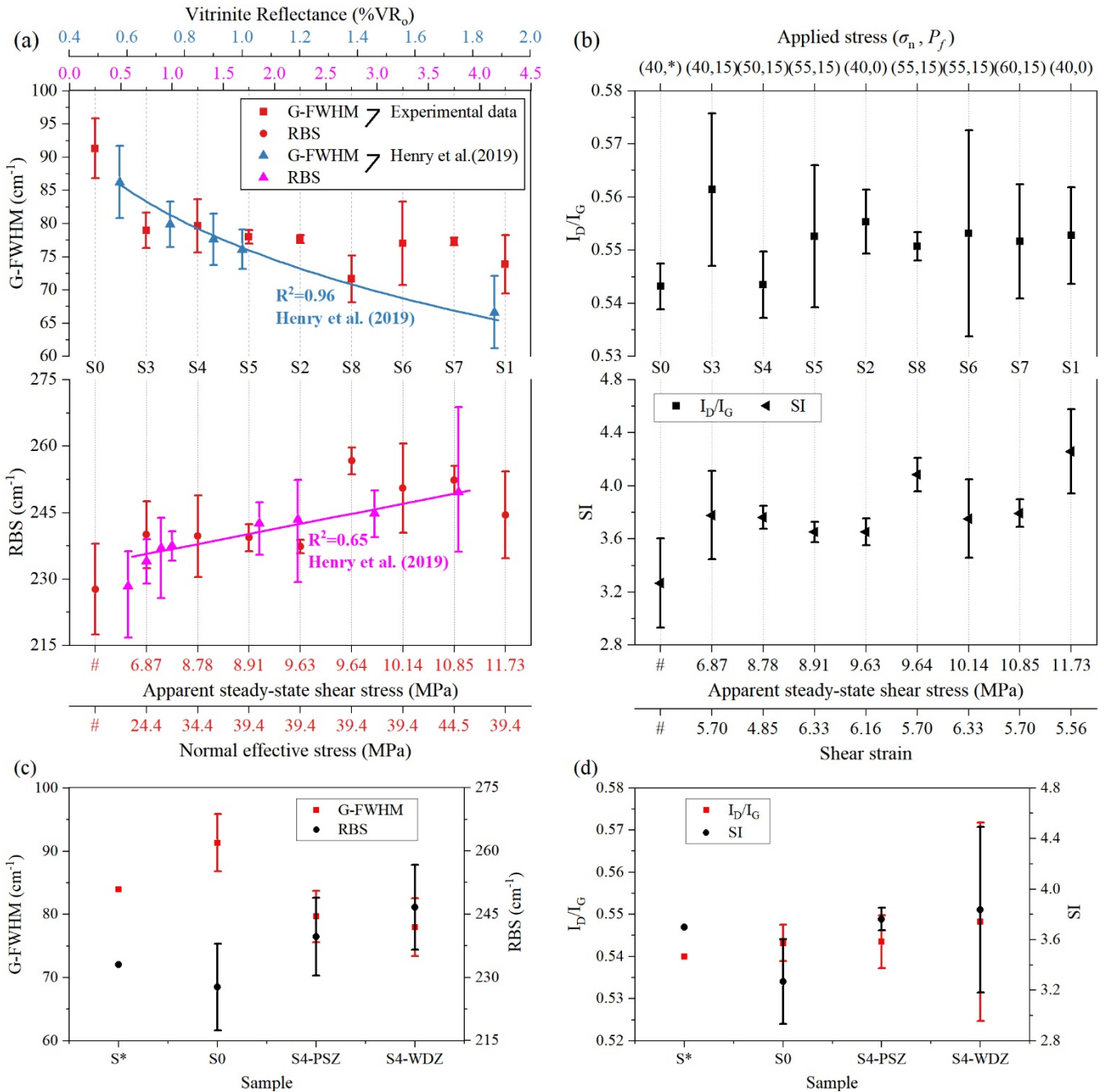
Figure 11: Representative Raman parameters as a function of apparent steady-state shear stress associated with shear strain measured at shear displacements of ~5.7 mm, plotted in (a) and (b). Note that the relation of G-FWHM vs. vitrinite reflectance and of RBS vs. vitrinite reflectance plotted in (a) were obtained from Henry et al. (2019). (c) and (d) show the difference of Raman parameters between S*, S0, S4-PSZ and S4-WDZ. The error bars are the standard deviations.
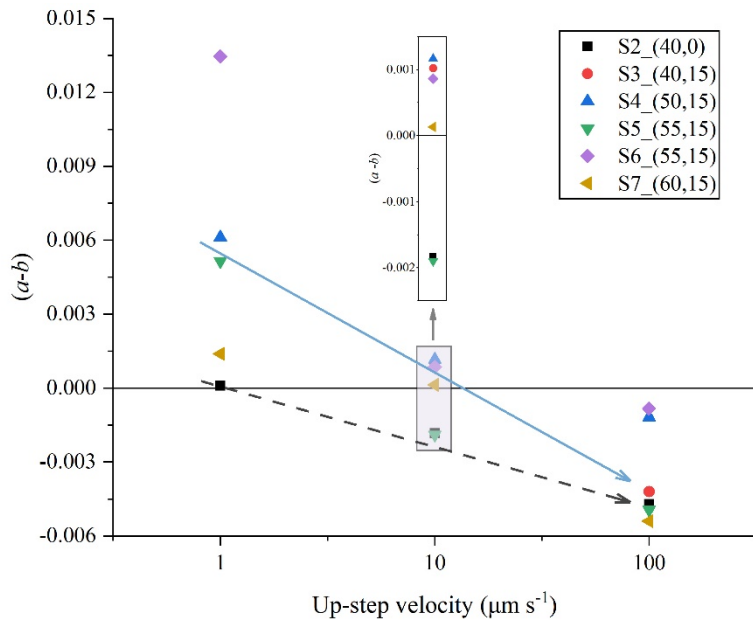
880

Figure 12: (*a-b*) values obtained from the experiments S2–S7 versus up-step velocity, showing a transition from velocity strengthening to velocity weakening.